Realizing Surface Driven Flows in the Primitive Equations

by

Eric Bembenek

A thesis
presented to the University of Waterloo
in fulfillment of the
thesis requirement for the degree of
Master of Math
in
Applied Mathematics

Waterloo, Ontario, Canada, 2014

Author's Declaration

I hereby declare that I am the sole author of this thesis. This is a true copy of the thesis, including any required final revisions, as accepted by my examiners.

I understand that my thesis may be made electronically available to the public.

Abstract

The surface quasi-geostrophic (SQG) model describes the evolution of buoyancy at vertical boundaries in the limit of infinitesimal Rossby number. In this regime, the quasi-geostrophic approximations are expected to hold. Numerical simulation of the SQG model often generate small-scale vortices which may have Rossby numbers that approach unity and may be outside the range of SQG. In this thesis we investigate the evolution of a surface trapped elliptical vortex in both the SQG model and the non-hydrostatic Boussinesq primitive equations (PE) which are better able to describe a wider range of oceanic dynamics. Thus, in the PE, we can vary the Rossby number in order to understand how the surface trapped vortex breaks down at the smaller-scale during its evolution. For small Rossby number, we confirm that the PE match the SQG prediction very well. For larger Rossby number however, we find that the models do not agree and different dynamics begin emerging in the PE. In particular, we find that the thin filament instability in the surface buoyancy field, common to SQG, begins to stabilize as the Rossby number increases and thus the emergence of the secondary small-scale vortices is halted. The core of the vortex spreads out and becomes much more uniform for larger Rossby number. The energy spectrum of the surface trapped vortex steepens from a power law of $-5/3$ to about -3 and the divergent energy grows as the Rossby number approaches unity. The growing divergent energy is an indication that inertia-gravity waves are generated in the simulation and we do indeed observe these in the vertical velocity field. We conclude that when the Rossby number of the surface trapped elliptical vortex is at least 0.05 new dynamics emerge and the PE must be used to attain an accurate description of the evolution of the flow.

Acknowledgements

First and foremost, I would like to thank my supervisors Dr. Francis Poulin and Dr. Michael Waite for their support and guidance throughout my thesis. Furthermore, I would like to thank the members of the Environmental and Geophysical Fluid Dynamics group for their insightful discussions and conversations (and many not so insightful discussions!) thoughout my thesis.

I would also like to thank my family and friends for their support throughout my thesis. I would like to thank the Godglicks, the Padaczs, and the McLeans. Thanks for all the laughter, intense Euchre games, and the great times we have shared together.

Dedication

To my parents who have supported me throughout my academic career

Table of Contents

List of Tables

List of Figures

Chapter 1

Introduction and Background

The surface quasi-geostrophic (SQG) model describes rapidly rotating, large scale, relatively slow moving flows whose motion is driven by surface buoyancy perturbations (due to temperature or salinity differences) at vertical boundaries (e.g [19], [23]). In nature, the SQG model can be used to describe the surface buoyancy of the ocean (e.g. [22], [25]). This model makes a few major assumptions regarding the flow and, therefore, can be limited in what oceanic flows it can describe accurately. As we shall see, this model is essentially two-dimensional and is quite inexpensive to solve numerically in comparison with three-dimensional models. Therefore, it is advantageous to use this model, assuming it is appropriate for the flow under consideration. The question then becomes: under what circumstances is the SQG model appropriate to use? To answer this, we can consider a more general model: the non-hydrostatic Boussinesq primitive equations (PE). The PE are very good at describing virtually all large-scale oceanic flows but they are three-dimensional and, as a result, can be very expensive to solve numerically. In this thesis, we compare numerical results of the SQG model to those of the PE and discuss when SQG is appropriate for describing large-scale oceanic flows and how the model breaks down at small-scales.

The outline for this thesis is as follows: in this chapter, we discuss the mathematical models used in this thesis, including the PE and the SQG models, and, once the models have been presented, we discuss some of the relevant research that has been done using the SQG model. In chapter 2, the numerical methods are presented and discussed along with the other tools used to compare and contrast the numerical results from the SQG and PE simulations using a surface trapped elliptical vortex. In chapter 3, we present results and analyze the output using the tools describe in chapter 2. Finally, chapter 4 concludes our findings and gives ideas about possible future work. The results of the

surface trapped elliptical vortex have been submitted as a manuscript to the Journal of Physical Oceanography and much of the thesis is based on the manuscript [3].

The thesis assumes knowledge of basic fluid mechanics and Fourier series. We assume the reader has knowledge of the stratified Euler equations in a rotating reference frame. Throughout the thesis, we use $\boldsymbol{v}$ to denote the full three-dimensional velocity fluid while $\boldsymbol{u}$ denotes the two-dimensional horizontal velocity field. The horizontal gradient and Laplacian are denoted by ∇_H, ∇_H^2 and the full three-dimensional gradient and Laplacian are denoted by ∇, ∇^2, respectively.

1.1 Mathematical Models of the Ocean

To describe oceanic flows, we turn to mathematics. While the Navier-Stokes equations are able to describe fluid flow from large-scale motions encountered in the atmosphere and oceans to small-scale flow in a cup of tea, we make use of the Euler equations, in particular, we consider the stratified Euler equations in a rotating reference frame. The key difference between the Navier-Stokes equations and the Euler equations is a lack of the viscosity term in the latter set of equations. The absence of this term is usually valid away from solid boundaries, in particular at the surface of the ocean away from the coasts.

We first discuss a common approximation to oceanic flows known as the Boussinesq approximation (e.g. [27], [46]). From there, we show how one can derive the quasi-geostrophic (QG) model and, going further, the SQG model.

1.1.1 The Boussinesq Approximation

The Boussinesq approximation is used to describe fluids with varying density and assumes that the variations in density are small compared to the mean density, as is true for the ocean (e.g. [27], [46]). To derive these equations, we begin with the stratified Euler equations in a rotating reference frame, given by,

$$\rho\left(\frac{D\boldsymbol{v}}{Dt} + \boldsymbol{f}\times\boldsymbol{v}\right) = -\nabla p - g\rho\hat{\boldsymbol{k}}, \tag{1.1}$$

$$\frac{\partial\rho}{\partial t} + \nabla\cdot(\rho\boldsymbol{v}) = 0, \tag{1.2}$$

where $\rho = \rho(x, y, z)$ is the density, $\boldsymbol{f}\times\boldsymbol{v}$ is the Coriolis acceleration (and $\boldsymbol{f} = f\hat{\boldsymbol{k}}$, where f is the Coriolis parameter and $\hat{\boldsymbol{k}}$ is the unit vector in the vertical), p is the pressure, and g is

acceleration due to gravity. Equation (1.1) is the conservation of momentum equation and (1.2) is the conservation of mass equation or the continuity equation [27]. Some algebra reveals that (1.2) can also be written as,

$$\frac{1}{\rho}\frac{D\rho}{Dt} + \nabla \cdot \boldsymbol{v} = 0. \tag{1.3}$$

The Boussinesq approximation decomposes the density field into a constant reference, vertically-varying background, and space and time dependent perturbation densities: $\rho = \rho_0 + \bar{\rho}(z) + \rho'(x, y, z, t)$. Further, we make the assumption that the deviations in density are small compared to the reference density: $|\rho_0| \gg |\bar{\rho}|, |\rho'|$ (e.g. [27], [46]). Similarly, we can decompose the pressure as $p = \bar{p}(z) + p'(x, y, z, t)$ and assume that,

$$\frac{d\bar{p}}{dz} = -g(\rho_0 + \bar{\rho}). \tag{1.4}$$

Decomposing the density and pressure in this way, we find that (1.1) can be simplified to,

$$\frac{D\boldsymbol{v}}{Dt} + \boldsymbol{f} \times \boldsymbol{v} = -\frac{1}{\rho_0}\frac{1}{1 + \bar{\rho}/\rho_0 + \rho'/\rho_0}\left(\nabla p' - g\rho'\boldsymbol{k}\right). \tag{1.5}$$

Due to the smallness of the background and perturbation densities, $1 + \bar{\rho}/\rho_0 + \rho'/\rho_0 \approx 1$. Furthermore, in equation (1.3), we take,

$$\nabla \cdot \boldsymbol{v} \gg \frac{1}{\rho}\frac{D\rho}{Dt}. \tag{1.6}$$

This assumption allows us to write the continuity equation as the incompressibility condition,

$$\nabla \cdot \boldsymbol{v} = 0. \tag{1.7}$$

The requirements for the incompressibility condition to hold can be found in numerous textbooks (e.g. [2], [27]). Letting U, L, H, and T denote the characteristic velocity, horizontal length, vertical length, and time scales, respectively, and c denote the speed of sound in the fluid medium, the conditions are [27]:

- The characteristic velocity in the flow is much smaller than the speed of sound in the fluid medium (i.e. small Mach number): $|U/c| \ll 1$
- The period of sound waves is much smaller than the characteristic time-scale in the flow: $T \gg L/c$

- The vertical length scale is not too large: $H \ll c^2/g$

In order to describe how the adiabatic density field evolves in time, we make use of the energy equation [27],

$$\frac{DT}{Dt} = 0, \tag{1.8}$$

where T is the temperature and we neglect compressibility and heat diffusion. By assuming a linear equation of state between density and temperature [27],

$$\rho = \rho_0(1 - \alpha(T - T_0)), \tag{1.9}$$

we can re-write the energy equation in terms of the density,

$$\frac{D\rho}{Dt} = \frac{D\rho'}{Dt} + \frac{d\bar{\rho}}{dz}w = 0. \tag{1.10}$$

We define the buoyancy field by re-scaling the density,

$$b = -g\frac{\rho}{\rho_0} \Rightarrow \bar{b}(z) + b'(x, y, z, t) = -g\frac{\bar{\rho}}{\rho_0} - g\frac{\rho'}{\rho_0}. \tag{1.11}$$

This substitution allows us to write the conservation of momentum equation as

$$\frac{D\boldsymbol{v}}{Dt} + \boldsymbol{f} \times \boldsymbol{v} = -\frac{1}{\rho_0}\nabla p' + b'\hat{\boldsymbol{k}}, \tag{1.12}$$

and the energy equation can be re-written in terms of buoyancy (in Vallis 2006 [46] this equation is also called the thermodynamic equation),

$$\frac{Db'}{Dt} + N^2(z)w = 0, \tag{1.13}$$

where,

$$N(z) = \sqrt{-\frac{g}{\rho_0}\frac{d\bar{\rho}}{dz}}, \tag{1.14}$$

is the buoyancy frequency. The buoyancy frequency is the frequency with which a particle, initially at rest and displaced vertically, oscillates. The PE are given by the set of equations (1.12), (1.7), and (1.13).

Variable	Scaling
(u, v)	U
w	W
(x, y)	L
z	H
t	L/U
p'	$\rho_0 fUL$
b'	fUL/H

Table 1.1: Scaling in the PE equations.

1.1.2 The Quasi-Geostrophic Equations

The QG model is an approximation to large-scale oceanic flow that is derived from the PE. It was first derived in Charney 1948 [8], however, for our derivation, we follow the details in Vallis 2006[46]. We first non-dimensionalize the PE. In table 1.1 we show the scaling assumptions made [46].

We scale the vertical velocity and length by a different scale compared to the horizontal velocities and lengths because we assume a small aspect ratio. The pressure and buoyancy are scaled as in table 1.1 due to assumed geostrophic and hydrostatic balance. To see this in detail, the pressure scale is chosen under the assumption that the Rossby number,

$$Ro = \frac{U}{fL}, \tag{1.15}$$

which gives the relative strength of rotation to advection, is very small. This implies that we have geostrophic balance (defined in (1.41)) and, therefore,

$$|\boldsymbol{f} \times \boldsymbol{u}| \sim |\frac{1}{\rho_0} \nabla_H p'|, \tag{1.16}$$

so that the scaling choice for pressure is,

$$p' \sim \rho_0 fUL. \tag{1.17}$$

To understand why buoyancy perturbations scale like fUL/H, we begin with hydrostatic balance. In large-scale oceanic flows, it is natural to assume a small aspect ratio. Therefore, we consider the case where $L \gg H$ and, using incompressibility in (1.7), find that the vertical velocity scales like,

$$W \sim U\frac{H}{L} \Rightarrow W \ll U. \tag{1.18}$$

If we consider the vertical momentum equation, after non-dimensionalizing, we find,

$$U^2 \frac{H^2}{L^2} \left(\frac{D\tilde{w}}{D\tilde{t}} \right) = fUL \frac{\partial \tilde{p}'}{\partial \tilde{z}} + B\tilde{b}', \tag{1.19}$$

where the overhead tilde denotes non-dimensional variables. Since $L \gg H$, this suggests that the vertical acceleration term is negligible and that the pressure term balances the buoyancy. The scaling for buoyancy is therefore,

$$B \sim fUL \frac{\partial p'}{\partial z} \sim \frac{fUL}{H}. \tag{1.20}$$

By transforming the physical variables to non-dimensional ones, one can write equations (1.12), (1.7), and (1.13) as

$$Ro \left(\frac{D\tilde{\boldsymbol{u}}}{D\tilde{t}} \right) + \hat{\boldsymbol{k}} \times \tilde{\boldsymbol{u}} = -\nabla \tilde{p}', \tag{1.21}$$

$$\frac{\partial \tilde{p}'}{\partial \tilde{z}} = \tilde{b}' \tag{1.22}$$

$$\tilde{\nabla}_H \cdot \tilde{\boldsymbol{u}} + \frac{\partial \tilde{w}}{\partial \tilde{z}} = 0, \tag{1.23}$$

$$Ro \, \frac{D\tilde{b}'}{D\tilde{t}} + \left(\frac{L_d}{L} \right)^2 \tilde{w} = 0, \tag{1.24}$$

where $L_d = NH/f$ is the Rossby radius of deformation. We have decomposed the momentum equation from (1.12) into the horizontal momentum equation (1.21) and vertical momentum equation under assumed hydrostatic balance (1.22).

The QG approximation assumes (e.g. [8], [46]) that

- Rotation dominates advection: $Ro \ll 1$
- Horizontal length scales are on the order of the Rossby radius of deformation: $L \sim L_d$
- Small aspect ratio: $L \ll H$

We note that the second assumption can be written in a number of ways. For example, the assumption can be written in terms of the Burger number,

$$Bu = \left(\frac{L_d}{L} \right)^2 = \left(\frac{NH}{fL} \right)^2 \sim 1. \tag{1.25}$$

The size of the Burger number implies that the Froude number,

$$Fr = \frac{U}{NH} \sim Ro\, \frac{L}{L_d} \ll 1. \tag{1.26}$$

Given the smallness of the Rossby number, one can perform an asymptotic expansion (e.g. [4]), by expanding the variables in an asymptotic series,

$$\tilde{\boldsymbol{v}} = \boldsymbol{v}_0 + Ro\, \boldsymbol{v}_1 + \mathcal{O}(Ro^2), \tag{1.27}$$
$$\tilde{b}' = b'_0 + Ro\, b'_1 + \mathcal{O}(Ro^2), \tag{1.28}$$
$$\tilde{p}' = p'_0 + Ro\, p'_1 + \mathcal{O}(Ro^2), \tag{1.29}$$

where the terms in the series expansion, $\boldsymbol{v}_i, p'_i, b'_i$, are understood to be non-dimensional. One then substitutes the series expansion into the non-dimensionalized PE in (1.21)-(1.24) and collects terms of the same order of Rossby number. As alluded to earlier, the leading order (that is, after collecting terms of $\mathcal{O}(1)$) horizontal momentum equation reduces to geostrophic balance,

$$v_0 = \frac{\partial p'_0}{\partial \tilde{x}}, \quad u_0 = -\frac{\partial p'_0}{\partial \tilde{y}}. \tag{1.30}$$

Using the energy equation (1.24), we find that, at leading order, $(L_d/L)^2 w_0 \sim 0$. Therefore, $w_0 = 0$. Alternatively, this can be derived using the leading order continuity equation (1.23) where, after integrating, we find that $w_0 = const.$ The constant is then specified by vertical boundary condition. We make the rigid lid approximation at the surface and assume a flat bottom. For vertical boundary conditions, we use the free-slip boundary condition which implies no normal flow. Therefore, $w_0 = 0$ everywhere. Using the vertical momentum equation, we find that the leading order buoyancy field is in hydrostatic balance as discussed during the start of this section,

$$b'_0 = \frac{\partial p'_0}{\partial \tilde{z}}. \tag{1.31}$$

By taking a vertical derivative of geostrophic balance in equation (1.30) and substituting hydrostatic balance, we find that the leading order buoyancy and horizontal velocity fields are in thermal wind balance (e.g. [46]),

$$\frac{\partial v_0}{\partial \tilde{z}} = \frac{\partial b'_0}{\partial \tilde{x}} \quad \text{and} \quad \frac{\partial u_0}{\partial \tilde{z}} = -\frac{\partial b'_0}{\partial \tilde{y}}. \tag{1.32}$$

These balance equations are useful and will be used to simplify the derivation of the QG model and the derivation of the ω equation (see section 2.3.1).

In order to describe how the system evolves in time, we consider the $\mathcal{O}(Ro)$ energy equation,

$$\frac{D_0}{D\tilde{t}}\left[\left(\frac{L_d}{L}\right)^2 b_0'\right] + w_1 = 0, \tag{1.33}$$

where w_1 is an unknown function and

$$\frac{D_0}{D\tilde{t}} = \frac{\partial}{\partial\tilde{t}} + \boldsymbol{u}_0 \cdot \tilde{\nabla}_H, \tag{1.34}$$

is the material derivative with advection due to the leading order geostrophic velocity (1.30). We note that, although $L_d = N(z)H/f$ (i.e. a function of z), we can absorb the ratio $(L_d/L)^2$ into the material derivative in (1.34) since there is no vertical differentiation present in $D_0/D\tilde{t}$. The challenge now becomes deriving a way to express the unknown function w_1 in terms of the known functions u_0, v_0, and b_0. This can be readily done by cross-differentiating the $\mathcal{O}(Ro)$ horizontal momentum equation and subtracting the resulting equations. This yields an evolution equation for the leading order vertical vorticity, $\zeta_0 = \partial_{\tilde{x}} v_0 - \partial_{\tilde{y}} u_0$. We find that the leading order vertical vorticity equation is,

$$\frac{D_0\zeta_0}{D\tilde{t}} = -\tilde{\nabla}_H \cdot \boldsymbol{u}_1. \tag{1.35}$$

The $\mathcal{O}(Ro)$ incompressibility equation reads,

$$\tilde{\nabla}_H \cdot \boldsymbol{u}_1 = -\frac{\partial w_1}{\partial\tilde{z}}. \tag{1.36}$$

We apply a vertical derivative to (1.33) and combine the result with (1.36) and (1.35) to find

$$\frac{D_0}{D\tilde{t}}\left[\zeta_0 + \frac{\partial}{\partial\tilde{z}}\left(\frac{L^2}{L_d^2} b_0'\right)\right] = -\left(\frac{L}{L_d}\right)^2 \frac{\partial \boldsymbol{u}_0}{\partial\tilde{z}} \cdot \tilde{\nabla}_H b_0', \tag{1.37}$$

where, using thermal wind balance in equation (1.32), we find

$$\frac{\partial \boldsymbol{u}_0}{\partial\tilde{z}} \cdot \tilde{\nabla}_H b_0' = \frac{\partial u_0}{\partial\tilde{z}}\frac{\partial b_0'}{\partial\tilde{x}} + \frac{\partial v_0}{\partial\tilde{z}}\frac{\partial b_0'}{\partial\tilde{y}} = -\frac{\partial b_0'}{\partial\tilde{y}}\frac{\partial b_0'}{\partial\tilde{x}} + \frac{\partial b_0'}{\partial\tilde{x}}\frac{\partial b_0'}{\partial\tilde{y}} = 0. \tag{1.38}$$

Therefore, at leading order, we have,

$$\frac{D_0}{D\tilde{t}}\left[\zeta_0 + \frac{\partial}{\partial\tilde{z}}\left(\frac{L^2}{L_d^2} b_0'\right)\right] = 0, \tag{1.39}$$

or, in dimensional variables,

$$\frac{D_g}{Dt}\left[\zeta + \frac{\partial}{\partial z}\left(\frac{f}{N^2(z)}b'\right)\right] = 0, \tag{1.40}$$

where $D_g/Dt = \partial_t + \boldsymbol{u}_g \cdot \nabla_H$ and $\boldsymbol{u}_g$ is the dimensional horizontal velocity due to geostrophic balance,

$$v = \frac{1}{f\rho_0}\frac{\partial p'}{\partial x}, \quad u = -\frac{1}{f\rho_0}\frac{\partial p'}{\partial y}. \tag{1.41}$$

One final substitution that we can perform on (1.40) is noting that, given geostrophic balance (1.41), one can introduce a streamfunction,

$$\psi = \frac{1}{f\rho_0}p'. \tag{1.42}$$

Furthermore, hydrostatic balance (1.31) allows one to relate buoyancy perturbations to the streamfunction via

$$b' = f\frac{\partial \psi}{\partial z}. \tag{1.43}$$

Thus, we can write all of the variables in (1.40) in terms of a single variable, the streamfunction,

$$\frac{D_g}{Dt}\left[\nabla^2\psi + \frac{\partial}{\partial z}\left(\frac{f^2}{N^2(z)}\frac{\partial \psi}{\partial z}\right)\right] = \frac{D_g q}{Dt} = 0 \text{ for } -H < z < 0, \tag{1.44}$$

where,

$$q \equiv \nabla^2\psi + \frac{\partial}{\partial z}\left[\left(\frac{f}{N(z)}\right)^2\frac{\partial \psi}{\partial z}\right], \tag{1.45}$$

is the QG potential vorticity (QG PV).

For vertical boundary conditions we make use of the energy equation (1.13) with the knowledge that at solid boundaries we assume the free-slip boundary condition. This implies that at vertical boundaries $w = 0$ and, therefore, (1.13) can be written as

$$\frac{D_g b'}{Dt} = 0 \text{ at } z = -H, 0. \tag{1.46}$$

There is a subtlety that can be overlooked here: the geostrophic velocities in the advection term of (1.46) are also computed at $z = -H, 0$. Thus (1.46) is really a two-dimensional evolution equation for the buoyancy perturbations.

The QG model is defined as the set of equations (1.44) and (1.46). In particular, in the interior of the fluid, $-H < z < 0$, the flow evolves according to (1.44) while at the vertical boundaries, $z = -H, 0$, the flow evolves according to (1.46). Furthermore, the relation between streamfunction and QG PV is given by (1.45) while the relationship between buoyancy perturbations and streamfunction is given by (1.43). The system has some interesting feedback characteristics in that the conserved quantities, q and b', are advected based on streamfunction and then the conserved variables, in turn, evolve the streamfunction and so on. It is also evident that there are a variety of research questions one can ask about this model. For this thesis, we reserve our study to the special case of SQG which will be described in the next subsection.

1.1.3 The Surface Quasi-Geostrophic Model

The SQG model describes the evolution of buoyancy perturbations at vertical boundaries (e.g. [19], [23], [43]). For our purposes, we also make the simplification that the surface buoyancy perturbations drive all motion in the fluid. Mathematically, this means taking the interior QG PV to be identically zero everywhere and neglecting all forces. While this is a strict approximation for the ocean, it is commonly used to focus on how the buoyancy evolves near the surface and it is a natural way to look at the effect of surface buoyancy on the interior of the fluid (e.g. [19], [43]). For boundary conditions, we let the surface buoyancy at $z = 0$ be some given field, $b'(x, y, 0, t) = b^t(x, y, t)$. At the bottom of the fluid, we take $b'(x, y, -H, t) = 0$. While the original SQG model in Held et al. 1995 [19] assumed a semi-infinite vertical domain, for our purposes we choose a finite vertical domain. The reason for this is two-fold. First, the ocean is finite and second, we wish to compare the numerical solutions of the SQG model to the PE, a three-dimensional model. The finite-depth model was first described in Tulloch and Smith 2006 [43]. By assuming periodic boundary conditions in the horizontal, we can decompose the streamfunction in terms of a Fourier series,

$$\psi(x, y, z) = \Re\left(\sum_{k=-\infty}^{\infty}\sum_{l=-\infty}^{\infty}\hat{\psi}(k, l, z)e^{i(kx+ly)}\right), \tag{1.47}$$

where $\Re$ denotes the real part of a quantity and we have suppressed the time-dependence for clarity. Therefore, setting $q = 0$ in equation (1.45), for each horizontal Fourier coefficient, we have,

$$-K^2\hat{\psi} + \frac{d}{dz}\left[\left(\frac{f}{N(z)}\right)^2\frac{d\hat{\psi}}{dz}\right] = 0, \tag{1.48}$$

where the carat symbol denotes horizontal Fourier coefficient and $K = \sqrt{k^2 + l^2}$ is the modulus of the horizontal wave-vector (k, l).

Constant Stratification

When the background stratification is non-constant (i.e. $N = N(z)$), finding an analytic solution to (1.48) for $\hat{\psi}$ can become difficult (see section 3.3). However, we can simplify the problem by assuming a linear background stratification which allows for an exact solution for the streamfunction in (1.48). A linear background stratification implies that $N = const.$ This simplifying assumption is commonly used (e.g. [19], [31], [43]). The solution to (1.48), in spectral space, for a single Fourier coefficient, is,

$$\hat{\psi} = A \sinh\left(\frac{NH}{f}(z+H)\right) + B \cosh\left(\frac{NH}{f}(z+H)\right). \tag{1.49}$$

After applying the boundary conditions, we find

$$\hat{\psi} = \frac{1}{NK} \frac{\cosh\left(\frac{NK}{f}(z+H)\right)}{\sinh\left(\frac{NKH}{f}\right)} \hat{b}^t. \tag{1.50}$$

The corresponding three-dimensional buoyancy field is found by multiplying (1.50) by f and taking a vertical derivative (i.e. computing (1.43)), giving,

$$\hat{b} = \frac{\sinh\left(\frac{NK}{f}(z+H)\right)}{\sinh\left(\frac{NKH}{f}\right)} \hat{b}^t. \tag{1.51}$$

This solution was first described in Tulloch and Smith 2006 [43]. Evaluating (1.50) at $z = 0$ gives the inversion formula,

$$\hat{b}^t = NK \tanh\left(\frac{NKH}{f}\right) \hat{\psi}. \tag{1.52}$$

For comparison, we show the solution to the semi-infinite vertical domain SQG model from Held et al. 1995 [19]. The bottom boundary condition in the semi-infinite vertical domain problem becomes $\psi \to 0$ as $z \to -\infty$ while the boundary condition at the surface

remains the same as in the finite-depth case. Solving equation (1.48) and applying the boundary conditions gives,

$$\hat{\psi} = \frac{\hat{b}^t}{NK} \exp\left(\frac{NK}{f} z\right), \tag{1.53}$$

and the inversion formula is,

$$\hat{b}^t = NK\hat{\psi}. \tag{1.54}$$

Comparing (1.50) and (1.53) we see that both solution decay exponentially away from the surface. However, we see that, depending on the parameter values in (1.50) and (1.52), this decay can occur more quickly and is anomalous compared to the solution in Held et al. 1995 [19]. By this we mean that the surface buoyancy field can be forced to decay much more quickly than it would with a semi-infinite domain where it is allowed to freely decay. The key parameter in (1.50) and (1.52) is the ratio $NH/f = L_d$. As described in Tulloch and Smith 2006 [43], if $K\ L_d \ll 1$, then we can approximate,

$$\tanh\left(\frac{NKH}{f}\right) \approx \frac{NKH}{f}, \tag{1.55}$$

and, therefore, the inversion relation is,

$$\hat{b}^t \propto K^2\hat{\psi}. \tag{1.56}$$

We recall that this is the same inversion relation for a two-dimensional fluid which can be described by conservation of vorticity (see the discussion in section 2.1.4 or e.g. [1], [27]). This tells us that features with $K\ L_d \ll 1$ (or features with horizontal length scales larger than L_d) behave similarly to two-dimensional conservation of vorticity.

In the other limit, if $K\ L_d \gg 1$ then

$$\tanh\left(\frac{NKH}{f}\right) \approx 1. \tag{1.57}$$

The inversion relation can then be approximated with

$$\hat{b}^t \approx NK\hat{\psi}. \tag{1.58}$$

This is the inversion relation in the semi-infinite domain SQG model in Held et al. 1995 [19] shown in (1.54). Therefore, features with $K\ L_d \gg 1$ (or features with horizontal length scales smaller than L_d) behave like the SQG model presented in Held et al. [19]. We can see that there is a transition between two-dimensional-like and SQG motion when $K\ L_d \sim 1$.

Because we wish to study purely SQG motion, we want to ensure that all structures in our simulation have $K\ L_d \gg 1$. Through experimentation, we found that by choosing $H = fL/N$, where L is the largest length scale in our initial conditions and H is the depth of fluid, we can ensure that all features behave according to pure SQG dynamics (i.e. minimizing finite-domain effects) without sacrificing too much vertical resolution.

1.1.4 Internal Gravity Waves

Since the SQG model is an approximation to the PE, some of the physical phenomenon which exist in the PE are not realizable in the SQG model. An example of this is inertia-gravity waves which can and are generated in the PE simulations but not in the SQG simulations. Here, we present a brief discussion of inertia-gravity waves which can be found in Kundu 2010 [27].

Since we cannot solve the fully non-linear system in equations (1.12), (1.7), and (1.13) (i.e. the PE), we linearize the equations in order to derive a dispersion relation. The dimensional linearized equations read,

$$\frac{\partial u}{\partial x} + \frac{\partial v}{\partial y} + \frac{\partial w}{\partial z} = 0, \tag{1.59}$$

$$\frac{\partial u}{\partial t} - fv = -\frac{1}{\rho_0}\frac{\partial p}{\partial x}, \tag{1.60}$$

$$\frac{\partial v}{\partial t} + fu = -\frac{1}{\rho_0}\frac{\partial p}{\partial y}, \tag{1.61}$$

$$\frac{\partial w}{\partial t} = -\frac{1}{\rho_0}\frac{\partial p}{\partial z} + b', \tag{1.62}$$

$$\frac{\partial b'}{\partial t} + N^2 w = 0. \tag{1.63}$$

Here, the only assumption that we make is that $N = const.$

Our goal is to write everything in terms of one variable. Specifically, we shall eliminate u, v, p, and b' in order to find one linear partial differential equation for the vertical velocity, w. One can show that the system of linear partial differential equations can be reduced to [27],

$$\frac{\partial^2}{\partial t^2}\nabla^2 w + N^2\nabla_H^2 w + f^2\frac{\partial^2 w}{\partial z^2} = 0. \tag{1.64}$$

In order to solve this equation, we assume that the vertical velocity can be decomposed into Fourier modes via,

$$w = \tilde{w}(z)e^{ik+il-\omega t}. \tag{1.65}$$

This decomposition simplifies the partial differential equation in (1.64) to an ordinary differential equation for each horizontal Fourier coefficient, $\tilde{w}$,

$$\frac{d^2\tilde{w}}{dz^2} + \frac{\omega^2K^2 - N^2K^2}{f^2 - \omega^2}\tilde{w} = 0. \tag{1.66}$$

We define,

$$m^2 = \frac{\omega^2K^2 - N^2K^2}{f^2 - \omega^2}. \tag{1.67}$$

At the vertical boundaries we have no normal flow and, therefore, $w = 0 \Rightarrow \tilde{w} = 0$ at $z = 0, -H$. There are two cases one can consider depending on the sign of m^2 in (1.67). If $m^2 < 0$, the solution to equation (1.66) are exponential in nature but it can be shown that no solutions exists given our choice of boundary conditions. If $m^2 > 0$ we can, again, write the vertical velocity in terms of Fourier modes, this time, a sine series. In particular, we let,

$$\tilde{w}(z) = \hat{w}\sin\left(\frac{\pi m z}{H}\right), \tag{1.68}$$

which satisfies the differential equation in (1.66) and the no normal flow boundary conditions.

By re-arranging (1.67) for ω we can find the dispersion relation for internal gravity waves. Namely, we find,

$$\omega^2 = \frac{N^2K^2 + f^2m^2}{K^2 + m^2}. \tag{1.69}$$

From the disperision relation (1.69), we note that the frequency of internal gravity waves is bounded by

$$f \leq \omega \leq N, \tag{1.70}$$

and, therefore, the period of gravity waves is bounded by,

$$\frac{2\pi}{N} \leq T_p \leq \frac{2\pi}{f}, \tag{1.71}$$

where T_p denotes the period. The bounds on the period of inertia-gravity waves is an important result and will be discuss further in the numerical approach discussion of section 2.1.5.

1.2 The Surface Quasi-Geostrophic Model in the Literature

Now that we have described what the SQG model is, we discuss how this model has been used to describe ocean dynamics and the various results that have been presented in the literature. While the SQG model in this thesis and other work (e.g. [29]) [31]), has been presented in the context of oceanic dynamics, it can also be used to describe some atmospheric dynamics (e.g. [23], [43], [45]).

The SQG model has some major assumptions: first, the model assumes zero interior QG PV and, second, a linear background stratification profile i.e. constant buoyancy frequency; nevertheless, it has been quite successful. For example, Le Traon et al. 2008 [32] argued that, in certain areas in the world, the SQG model agrees better with ocean data compared to QG theory which describes evolution of interior QG PV. Their discussion was based on the predicted energy spectra of turbulent flow in the SQG model and QG model compared to the wavenumber spectra measured by altimeter data in the Gulf Stream, Kuroshio, and Agulhas regions. They argued that the predicted energy spectra in the SQG model was a better match than the predicted energy spectra of the QG model.

Rocha et al. 2013 [38] showed that SQG was consistent with a four-QG-mode combination in the Southwestern Atlantic. In particular, they showed that using a combination of the barotropic, 1st, 2nd, and 3rd baroclinic QG modes showed very good agreement with the SQG model. QG modes are a set of vertical basis functions for QG PV that are found by solving the eigenvalue problem in (1.45) by assuming a seperation of variables. The barotropic mode is constant in z while the n-th baroclinic modes are cosine modes,

$$\phi_n(x) = \cos\left(\frac{n\pi z}{H}\right). \tag{1.72}$$

For a further discussion on QG-modes, see Vallis 2006 [46]. This suggests that one can use the relatively simple SQG model instead of the more complicated four-QG-mode combination, at least in the Southwestern Atlantic, and find good agreement with data gathered there.

Tulloch and Smith 2006 [43] showed that the finite depth SQG model (discussed in detail in section 1.1.3 and used in this thesis) is able to attain a horizontal kinetic energy spectrum with a power law of $K^{-5/3}$ at small scales (i.e. for $K\ L_d \gg 1$) and K^{-3} at large scales (i.e. for $K\ L_d \ll 1$) with a smooth transition in-between. This result is significant in that the Global Atmospheric Sampling Program data has a spectral shape that resembles what arises in the kinetic energy spectrum in the finite-depth SQG model [36]. Tulloch

and Smith 2006 [43] argued a full understanding of why the data forms this spectral shape must include finite depth SQG dynamics.

In regards to the assumptions of zero QG PV and constant buoyancy frequency, Lapeyre and Klein 2006 [31] showed that using an "effective" SQG model, one is able to match data quite well with flows with non-constant buoyancy frequency and even flows which had non-zero QG PV near the surface. Far enough away from the surface, however, the model has trouble matching observed data. The effective SQG model chooses the buoyancy frequency, N, not from a physical description, but in order to match data closely near the surface. In their paper, an algorithm is described in how one chooses N appropriately. From there, one uses the exponentially decaying solution found in Held et al. 1995 [19] and stated in (1.53) and (1.54). The effective SQG [31] model supports our use of constant N and the assumption of zero QG PV. Furthermore, the effective SQG model has been used in other studies to describe oceanic dynamics. For instance, in Isern-Fontanet et al. 2008 [22], it is shown that the effective SQG model, compared to an Ocean General Circulation model simulation, is quite accurate in matching the surface velocity field. Furthermore, it is shown that it does a reasonable job matching the velocity field in the upper 500 m. In Klein et al. 2009 [25], it was, again, found that the effective SQG model was accurate compared to a PE solution in reconstructing velocities at the surface and down to a depth of 500 m.

While SQG has seen success there is a well-known limitation in the model. In particular, numerical simulations of SQG more often than not generate small scale vortices and eddies which are beyond the extent of SQG (e.g. [19], [23]). The SQG model assumes an infinitesimal Ro for all structures generated in the simulation. However, the Rossby number of these structures increases as $Ro(K) \sim K^{2/3}$ (e.g. [10], [23]). To see this, we can consider how the Rossby number depends on horizontal wavenumber,

$$Ro(K) \sim \frac{U(K)}{L(K)}. \tag{1.73}$$

Clearly, $L(K) \sim K^{-1}$ and the horizontal velocity scales like $U(K) \sim \sqrt{KE(K)}$ where $E(K)$ is the energy spectrum. The predicted energy spectrum, $E(K)$, of turbulence in the SQG model is $K^{-5/3}$ which is derived in Pierrehumbert et al. 1994 [37] and further discussed in Held et al. 1995 [19]. Therefore, we find that the horizontal velocity scales like $U(K) \sim K^{-1/3}$, so that

$$Ro(K) \sim K^{2/3}. \tag{1.74}$$

Thus, the dynamics in the SQG model generate features whose Rossby number grows like $K^{2/3}$. For large enough wavenumber (or small enough length scale), there is a breakdown of

the assumptions of SQG and the model is no longer valid. To understand how these small scale structures are actually evolving, we compare the results of numerical simulations of SQG to the PE.

Studies comparing SQG to the PE based on simulations have been discussed in the literature and we will discuss some of the more relevant results. Snyder et al. 2007 [40] discussed a surface trapped vortex dipole chosen to represent a localized jet. This particular setup does not generate any of the small-scale features that have been discussed within this section of the thesis but one of the main results in the paper is regarding the inertia-gravity waves that are generated. They argue that gravity waves are generated during the initial part of the numerical simulation if one uses an unbalanced initial setup. Specifically, if one uses initial conditions taken directly from the SQG solution (i.e. the leading order solution) in the PE then gravity waves will be generated during the early stages of the simulation. Danioux et al. 2012 [10] discussed spontaneous generation of inertia-gravity waves in the PE for surface-intensified turbulence. Their simulation showed that gravity waves tend to be emitted when the local Rossby number is $\mathcal{O}(1)$.

While SQG is the leading order solution in the asymptotic expansion to the PE, an SQG+1 model, which includes the $\mathcal{O}(Ro)$ corrections in the asymptotic derivation is derived in Hakim et al. 2002 [17] and Rotunno et al. 2000 [39].

For this thesis, we focus on the dynamics of a rotating elliptical surface trapped vortex in the SQG model and the PE. For the PE, we shall vary the Rossby number of the initial conditions in order to understand how the dynamics change for larger Rossby number where the SQG model's assumptions break down. Isolated vortices have been studied in detail by Held et al. 1995 [19], who presented the surface trapped elliptical vortex as their first example of SQG dynamics, Carton 2009 [7], and Dritschel 2011[12]. The latter two papers discussed the stability of surface trapped elliptical vortices.

Chapter 2

Methodology

2.1 Numerical Methods

In order to find solutions to the SQG model and the PE we turn to numerical methods. The components that we will discuss in computing a numerical solution are spatial discretization and derivatives, time-stepping, and small-scale dissipation. We present basic details on each of these topics.

2.1.1 Spatial Derivatives using the Pseudospectral Method

Periodic Boundary Condition

In order to compute derivatives accurately, we can make use of the pseudospectral method. First, however, in the spectral method (e.g. [13], [42]), the basic idea is to express the numerical solution, say U, in terms of a series of known orthogonal basis functions,

$$U(x,t) = \sum_{n=-N/2}^{N/2} a_n(t)\phi_n(x). \tag{2.1}$$

Generally, the choice of basis functions, $\phi_n(x)$, depends on the boundary conditions. Following Durran 1999 [13], for periodic boundary conditions, we choose $\phi_n(x) = e^{inx}$, i.e., a Fourier decomposition. The differential equation is written entirely in terms of the Fourier coefficients by assuming that the residual is orthogonal to the basis functions (e.g. [13]).

In contrast, the pseudospectral method sets the residual to zero at the grid points, and therefore only refers to the Fourier coefficients when computing derivatives (e.g. [13]; alternatively, the pseudo-spectral method can be derived using band limited interpolation, see [42]). The details can be found in numerous textbooks (e.g. [13], [42]). To compute a spatial derivative of some function u, we take the Discrete Fourier Transform (DFT) of $\partial_x u$ with the knowledge that spatial derivatives become algebraic multiplication in spectral space. From there, we invert back into physical space and take the real part of the inverse DFT. Mathematically, we have,

$$\frac{\partial u}{\partial x} = \Re(F^{-1}(ikF(u))), \tag{2.2}$$

where F and F^{-1} denote the Fourier transform and inverse Fourier transform, respectively.

While this method is very accurate for computing derivatives, its applicability is somewhat limited in that one must use periodic boundary conditions. However, by performing an even extension of a non-periodic function, one can use a Discrete Cosine Transform (DCT). The extra requirement here though is the Neumann boundary condition on u, v, and b' which is required to ensure that a cusp does not appear about the point we are performing the even extension (i.e. this would make the function not differentiable at this point and would introduce error when trying to compute its derivative). The drawback of the Neumann boundary condition for our study of SQG dynamics in the PE and is discussed further in section 2.1.5.

Non-Periodic Boundary Condition

For non-periodic boundary conditions, one possible series expansion is to use Chebyshev polynomials (e.g. [5], [42]). Chebyshev polynomials are defined, in Trefethen 2000 [42], as

$$T_n(x) = \Re(z^n) = \frac{1}{2}(z^n + z^{-n}), \tag{2.3}$$

where z is a complex number with $|z| = 1$. One can also define Chebyshev polynomials recursively,

$$T_{n+1}(x) = 2xT_n(x) - T_{n-1}(x), \tag{2.4}$$

with the base cases defined as $T_0(x) = 1$ and $T_1(x) = x$. An alternate definition [42] is

$$T_n(x) = \cos(n \cos^{-1}(x)), \tag{2.5}$$

which suggests using a change of variables,

$$\theta = \cos^{-1}(x). \tag{2.6}$$

Therefore, the n-th Chebyshev polynomial can be defined as

$$T_n(\theta) = \cos(n\theta). \tag{2.7}$$

This implies that the series expansion can be written in terms of a cosine series and, therefore, we can use a DCT to transform the function into spectral space and compute accurate derivatives.

This choice of series expansion uses a non-uniform grid which clusters points near the boundary. The grid is defined by,

$$x_j = \cos(\theta_j) = \cos(j\pi/N), \quad \text{for } j = 0, 1, \ldots, N, \tag{2.8}$$

where N is the number of grid points and a schematic diagram is shown in figure 2.1.

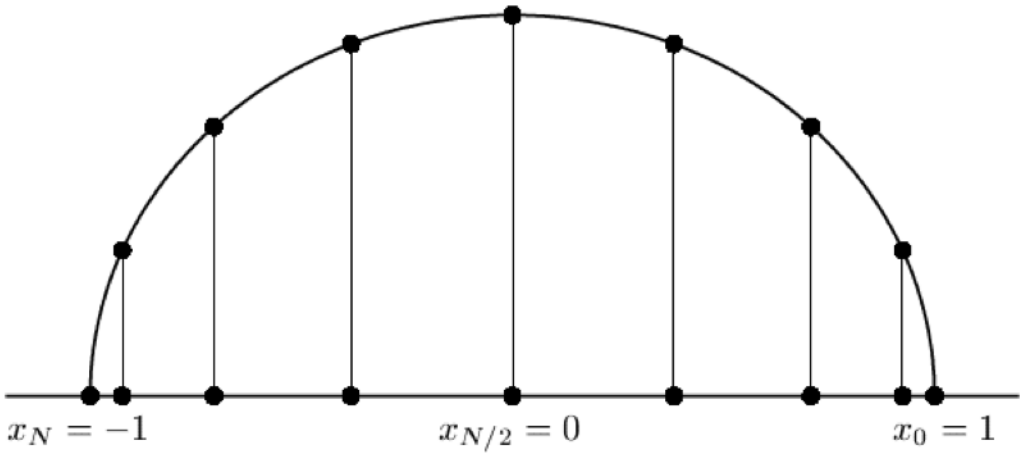

Figure 2.1: Projection of cosine points onto a clustered grid. Image from Trefethen 2000 [42].

The clustering of grid points allow for increased resolution near the boundary but the resolution in the interior is relatively coarse as a result. Increasing the number of grid points in order to improve resolution in the interior can be detrimental since it would force

a smaller time-step due to the Courant-Frederichs-Lewy (CFL) condition (e.g. [13]) which stipulates a requirement to ensure stability of the numerical solution. However, increasing the number of grid points near the surface is not necessarily a detriment for our study since most of the dynamics in the SQG model occur near the solid boundary at the surface.

2.1.2 Time-Stepping

Time-stepping is an important process that allows one to evolve their solution forward in time. For simplicity, suppose we are trying to solve the differential equation,

$$\frac{d\phi}{dt} = F(\phi). \tag{2.9}$$

There are a variety of different time-differencing methods one can use (see Durran 1999 [13]), however, both numerical models used in this thesis use the third-order Adams-Bashforth scheme, a linear multistep method, given by,

$$\phi^{n+1} = \phi^n + \frac{\Delta t}{12}\left[23F(\phi^n) - 16F(\phi^{n-1}) + 5F(\phi^{n-2})\right], \tag{2.10}$$

where Δt is the time-step and $\phi^n \approx \phi(n\Delta t)$ i.e., ϕ^n is the numerical solution at $t = n\Delta t$. This method requires the numerical solution, ϕ^n, from two earlier time steps and so storage can be an issue. However, we do find that the truncation error is $O(\Delta t^4)$ and is therefore quite accurate.

2.1.3 Small-Scale Filtering

Since we cannot resolve down to the scale where physical viscosity becomes important, we must remove energy from the smallest scales that our grid allows. To do this, we use an exponential filter that mimics hyperviscosity (e.g. [5]). The general form of the exponential filter is

$$s(k) = e^{-\alpha|k|^\beta}, \tag{2.11}$$

where k is wavenumber and α and β are parameters that we can vary. The filter is applied in spectral space and decreases the magnitude of Fourier coefficients with large wavenumbers (i.e. small-scales). Mathematically, to filter a variable, q, we compute its Fourier coefficients using the DFT, multiply by the filter, and transform back into physical space using the inverse DFT and take the real part:

$$q_f = \Re(F^{-1}(s(k)F(q))), \tag{2.12}$$

where q_f is the filtered variable.

The reason this exponential filter is considered to mimic hyperviscosity is clear when one considers a diffusion equation with hyperviscosity,

$$\frac{\partial u}{\partial t} = (-1)^{p+1}\nu\nabla^{2p}u, \tag{2.13}$$

where ν is the hyperviscosity coefficient and p is a positive integer. For a single Fourier coefficient, this implies,

$$\frac{d\hat{u}}{dt} = -\nu K^{2p}\hat{u}, \tag{2.14}$$

and has solution,

$$\hat{u} = \hat{u}_0 \exp(-\nu K^{2p} t). \tag{2.15}$$

where $\hat{u}_0(K)$ are the Fourier coefficients of the initial conditions, $u(x,0) = u_0(x)$. For a time interval of length Δt, this implies

$$\hat{u} = \hat{u}_0 \exp(-\nu \Delta t K^{2p}), \tag{2.16}$$

here, we identify that $\alpha = -\nu\Delta t$ and $\beta = 2p$. Therefore, we note that the filter strength depends on the size of the time-step, Δt.

Comparing (2.15) and (2.16) to (2.11) suggests that the effects of the exponential filter mimic that of hyperviscosity. Generally, the hyperviscosity allows for p be a positive integer, however, with the filter in (2.11), we can let both α and β to be real numbers since the filter only acts in spectral space. In order to choose appropriate parameter values, α and β, we think of the problem in a different way. In particular, we ask the question, at what wavenumber do we wish the filter to start decreasing the magnitude of their respective Fourier coefficients and at what wavenumber do we want the magnitudes to be reduced by half? Mathematically, we set,

$$s(k_m) = 0.9 = e^{-\alpha k_m^{\beta}}, \tag{2.17}$$

$$s(k_s) = 0.5 = e^{-\alpha k_s^{\beta}}, \tag{2.18}$$

where k_m and k_s denote the wavenumbers at which the filter reduces 10% and 50 % of the corresponding Fourier coefficients' magnitude, respectively. We can solve (2.17) and (2.18) to find α and β in terms of k_m and k_s. Some algebra reveals,

$$\alpha = 0.69 k_s^{-1.88/\ln\left(\frac{k_s}{k_m}\right)}, \tag{2.19}$$

$$\beta = \frac{1.88}{\ln\left(\frac{k_s}{k_m}\right)}. \tag{2.20}$$

This allows us to pick α and β in a way that is easily understandable.

2.1.4 QG3

In order to compute solutions to the SQG model, we make use of the numerical model QG3 written by Glenn Flierl (priv. comm.). In general, the code is able to solve multilayer problems of the form,

$$\frac{\partial \boldsymbol{\theta}}{\partial t} + J(\boldsymbol{\psi}, \boldsymbol{\theta}) = 0, \tag{2.21}$$

where $\boldsymbol{\theta}$ is a vector of any materially conserved quantities, and $\boldsymbol{\psi}$ is the corresponding vector of streamfunctions. Each component of $\boldsymbol{\theta}$ and $\boldsymbol{\psi}$ depend on the horizontal directions (and time) only. Here, we use the Jacobian notation, $J(A, B) = A_x B_y - A_y B_x$. The other requirement is a so-called inversion relation in spectral space between the conserved quantities, $\boldsymbol{\theta}$, and streamfunctions, $\boldsymbol{\psi}$,

$$\hat{\boldsymbol{\theta}} = M\hat{\boldsymbol{\psi}}, \tag{2.22}$$

where M is a matrix which stores the inversion relations. The inversion relations are derived from the physics of the system one is studying. Note that (2.22) is for the multilayer problem. For a single layer (as in SQG), M is a scalar function which gives the inversion relation between conserved quantity and streamfunction.

As an example of an inversion relation, if we consider two-dimensional fluid flow described by the Euler equations, we can write the dynamics as a conservation of vertical vorticity (e.g. [1], [27]),

$$\frac{\partial \zeta}{\partial t} + J(\psi, \zeta) = 0. \tag{2.23}$$

Furthermore, we know that the relationship between the vorticity and streamfunction are given by $\zeta = \nabla\psi$ or, in spectral space, the inversion relation is given by,

$$\hat{\zeta} = -K^2\hat{\psi}. \tag{2.24}$$

For SQG, the inversion relation is defined in (1.52).

QG3 uses the pseudospectral method with a Fourier series expansion to compute horizontal derivatives and uses the third-order Adams-Bashforth time-stepping scheme. The exponential filter is applied radially in spectral space. Time-stepping in QG3 is fixed at around $\Delta t = 5$ minutes. The grid spacing is $\Delta x \approx 390$ m with 512×512 grid points which spans a domain of 200 km $\times$ 200 km. The numerical model is run in serial on a desktop and the runtime is around 10 minutes.

2.1.5 SPINS

To solve the PE we make use of the Spectral Parallel Incompressible Navier-Stokes (SPINS) written by Subich et al. 2013 [41]. As with QG3, SPINS is a pseudospectral solver with third-order Adams-Bashforth time-stepping and can describe the dynamics of the PE. SPINS is parallelized using the Message Passing Interface (MPI) package and is run using Sharcnet computing resources. In general, using MPI allows one to use multiple processors, each solving a portion of the full domain. The result can be a dramatic speed-up in computation. For a description of how SPINS uses MPI see Subich et al. 2013 [41].

While SPINS uses an adaptive time-step to satisfy the CFL condition based on the momentum equation, we used a constant time-step. By allowing an adaptive time-step, we found spurious oscillations in the three-dimensional velocity and buoyancy fields. These oscillations are presented in figure 2.2 where we plot the xz cross-section of the vertical velocity through the center of the y axis. In panel (a), we plot the vertical velocity at $t = 1$ day and in panel (b) we plot the vertical velocity at $t = 4$ days. We choose a simulation with a very small Rossby number, $Ro = 0.005$ (for more details see section 3.1) because, as will be seen in chapter 3, this case matches very well with SQG. We can see spurious oscillations generated near the surface with relatively large velocities (indeed, as presented in chapter 3, all of the cases we discuss have vertical velocities 3-4 orders of magnitude smaller than these spurious oscillations). The velocities persist throughout the course of the simulation and affect the evolution of the surface buoyancy (not shown). We conclude that these oscillations are the result of numerical error.

These spurious oscillations are a results of the fact that the time-step chosen based on the CFL condition does not properly resolve gravity waves. To properly resolve these waves, we note that from section 1.1.4, the shortest period of inertia-gravity waves was found to be $T = 2\pi/N$ (see equation (1.71)). For the value of N we use, found in table 3.1, the shortest period is around 600 seconds. Therefore, in order to properly resolve these waves, we fix $\Delta t = 60$ seconds. It can also be argued that since the time-step has been reduced, this has the effect of increasing the strength of the filter (see 2.1.3, in particular equation (2.16)). However, after spending a great deal of time trying stronger filter parameters and finding these waves still being generated, albeit with larger wavelengths, the author believes that the more likely reason has to do with the resolving gravity waves.

We use $512 \times 512 \times 512$ grid points. The high number of vertical grid points is chosen based on the result in Tulloch and Smith 2009 [44] which states that in order to resolve wavenumber K, we need,

$$\Delta z \leq 0.3 \frac{f}{N} \frac{1}{K}. \tag{2.25}$$

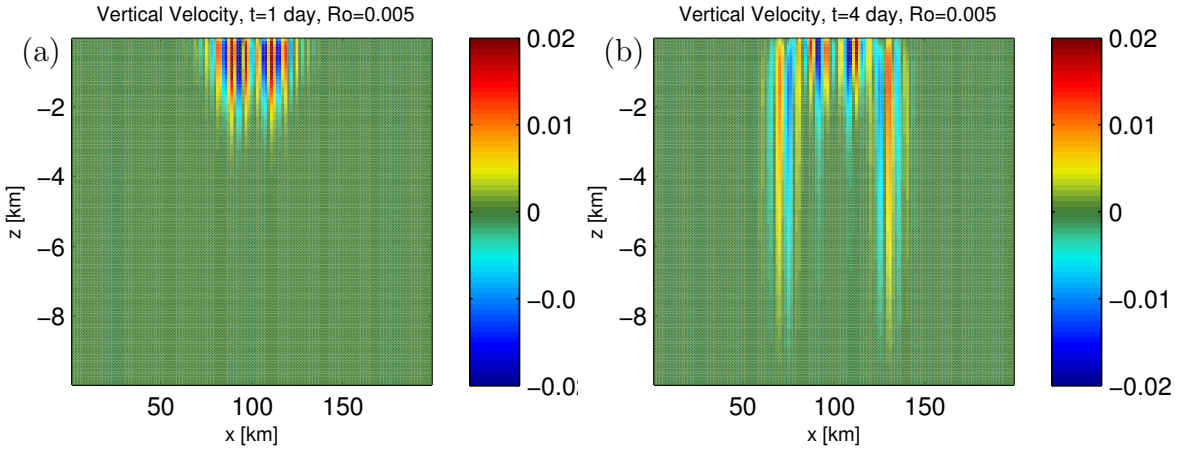

Figure 2.2: Vertical velocity at $t =$ (a) 1 day and (b) 4 days. The simulation used the adaptive time-step based on the CFL condition from the momentum equation.

The second reason for the high number of vertical grid points is that SPINS uses a staggered grid. Since we want to study the dynamics at the surface, we need to try to minimize Δz which, for a fixed depth, is done by increasing the number of grid points. Depending on the number of processors used to compute the solution up to 20 days on Sharcnet, we found the runtime to vary between about 3 days (if we used 64 processors) to about 5 days (if we used 32 processors).

For vertical boundary conditions, SPINS has three options: periodic, no-slip, and free-slip. The periodic boundary condition, which we use in the horizontal directions, uses DFT to compute derivatives implemented using FFTW [14]. The no-slip vertical boundary condition imposes that all velocities are zero at vertical solid boundaries and therefore won't be used in this thesis. Finally, the free-slip vertical boundary condition gives us the option to use a uniform grid or Chebyshev grid. In order to compute vertical derivatives in the uniform grid, SPINS uses a DCT on u, v, and b'. For the vertical velocity on the other hand, SPINS uses a Discrete Sine Transform (DST). The DCT forces the vertical boundary condition to impose an additional Neumann boundary conditions for u, v, and b'. Alternatively, we can use a Chebyshev grid. This has an advantage over the uniform grid in that there is a clustering of grid points near solid boundaries, particularly near the surface where we expect most of the dynamics to occur. Derivatives are then computed by a change of variables and then using a DCT (see Subich et al. (2013) [41] and section 2.1.1).

The exponential filter in SPINS is performed separately in each spatial direction. This is a slight difference to the filtering in QG3 and makes for some discrepancies in the smallest scales. Note also that there is no vertical dissipation in the QG3 model. In SPINS, the filtering is of the form

$$s(k) = \begin{cases} 1 & \text{if } k < k_c \\ \exp\left(-\alpha \left(\frac{|k|-k_c}{k_{\max}-k_c}\right)^{\beta}\right) & \text{if } k \geq k_c \end{cases}, \tag{2.26}$$

where $k_{\max} = \pi/\Delta x$ and k_c is the "cut-off" wavenumber. By setting $k_c = 0$, we find that the exponential filter is applied to all Fourier coefficients and is of the form of the hyperviscosity-like filter in (2.11).

2.2 Energy Spectra

To quantify some differences between the SQG and PE solutions, we make use of energy spectra. Energy spectra allows one to quantify how much energy is present at each length scale. Furthermore, there are theories for turbulent energy spectra that allow one to make a prediction of the fluid flow from a purely theoretical perspective.

We first present a derivation of the enery spectra that can be found in numerous textbooks (e.g. [11], [33]), then present how to compute the energy spectrum in practice, and, finally, discuss the predicted energy spectra in SQG.

2.2.1 Energy Spectrum from Turbulence Theory

Here, we follow the derivation in Lesieur 2008 [33] and that of the AM900 course on instability and turbulence [48] for a two-dimensional fluid. The reason for this is that SQG is anisotropic in the z direction, while in the horizontal, isotropy can be realizable.

The total horizontal kinetic energy at the surface (i.e. a two-dimensional slice) is given by

$$E = \frac{1}{L^2} \iint_{L^2} \frac{1}{2} \left(u^2 + v^2\right) dV, \tag{2.27}$$

or, using Parseval's Relation,

$$E = \sum_{k=-\infty}^{\infty} \sum_{l=-\infty}^{\infty} \frac{1}{2} \left(|\hat{u}|^2 + |\hat{v}|^2 \right). \tag{2.28}$$

We can write this as an integral over continuous wavenumber by multiplying (2.28) by $1 = (L/2\pi)^2(\Delta k)^2$. We define $\hat{U}(\boldsymbol{k}, t) = 1/2(|\hat{u}|^2 + |\hat{v}|^2)(L/2\pi)^2$ and take the limit as $\Delta k \to 0$. This limit corresponds to going from a finite domain to an unbounded domain. Thus, Fourier coefficients become Fourier transforms. These steps make (2.28) a Riemann sum and taking the limit gives,

$$E = \iint_{\boldsymbol{k}} \hat{U}(\boldsymbol{k}, t) d\boldsymbol{k}. \tag{2.29}$$

Note the domain of integration in (2.29) is taken to be $(k, l) = (-\infty, \infty) \times (-\infty, \infty)$. We make the assumption that, on average (i.e. ensemble or time-averaged), the dynamics are isotropic in the horizontal. This implies that $\hat{U}$ depends on the magnitude of the wavevector, $\hat{U}(\boldsymbol{k}, t) \to \hat{U}(K, t)$, and allows us to simplify the integral in (2.29). Using polar coordinates, one can show,

$$E = \int_0^{2\pi} \int_0^{\infty} K\hat{U}(K, t) dK d\theta = \int_0^{\infty} 2\pi K\hat{U}(K, t) dK. \tag{2.30}$$

Finally, we define the energy spectrum as,

$$E(K, t) = 2\pi K\hat{U}(K, t), \tag{2.31}$$

which is interpreted as the amount of energy (per unit wavenumber) present between wavenumbers K and $K + dK$. That is, it quantifies how much energy per unit wavenumber is present at each particular length scale. The full horizontal kinetic energy is then integrated over all wavenumbers,

$$E = \int_0^{\infty} E(K, t) dK. \tag{2.32}$$

2.2.2 Energy Spectrum in Practice

The above derivation assumed an infinite domain along with integrating in polar coordinates. However, our simulations are not in an infinite domain and, for simplicity, we

instead choose to integrate in Cartesian wavenumber coordinates. Furthermore, due to the discretization of our data, we approximate integrals with summations.

First, we consider a thin circular shell in spectral space, depicted in figure 2.3, centered at $K = K'$ and of width ΔK, called $S_{K'}$. Mathematically, we define the shell as,

$$S_{K'} = \left\{ \boldsymbol{k} \mid K' - \frac{\Delta K}{2} \leq |\boldsymbol{k}| \leq K' + \frac{\Delta K}{2} \right\}. \tag{2.33}$$

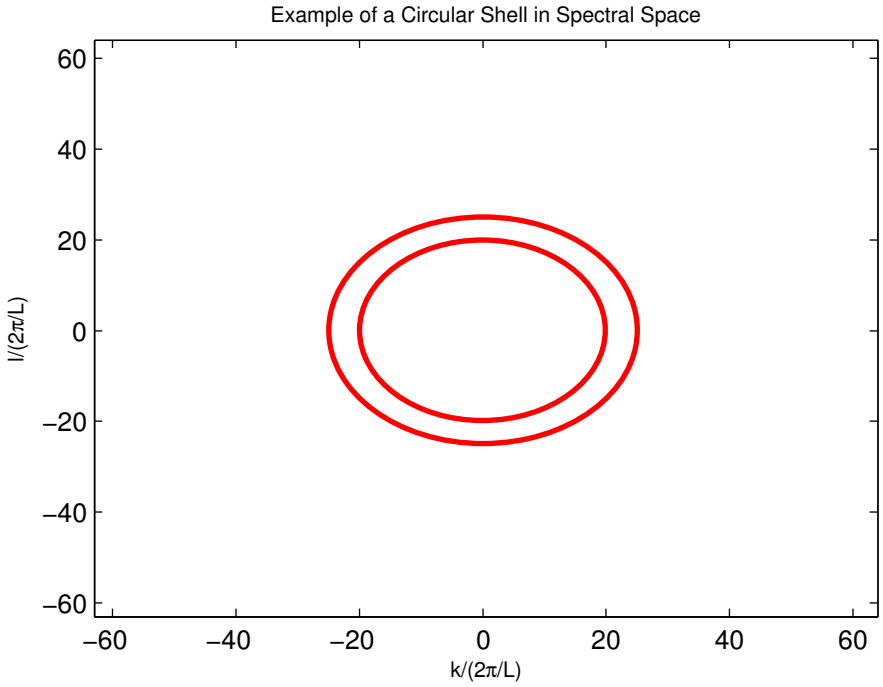

Figure 2.3: A schematic in spectral space of a circular shell.

The amount of energy within the shell can be calculated as an integral, which we approximate as,

$$E_{S_{K'}} = \int_{S_{K'}} E(K) dK \approx E(K') \Delta K. \tag{2.34}$$

Furthermore, using Parseval's relation, the energy can also be defined as a sum of Fourier coefficients,

$$E(K') \Delta K \approx \sum_{\boldsymbol{k} \in S_{K'}} \frac{1}{2} \left(|\hat{u}|^2 + |\hat{v}|^2 \right). \tag{2.35}$$

In practice, we simply sum the horizontal kinetic energy of each of the Fourier coefficients within the circular shell. This "binning" process is repeated for all of the other shells in the spectral domain. The interpretation of (2.35) is the amount of horizontal kinetic energy in the wavenumber range $(K' - \Delta K/2, K' + \Delta K/2)$.

We can also make use of the Helmholtz decomposition to write the horizontal velocity field as a divergent (or curl-free) part and rotational (or divergence-free) part. Some algebra reveals that,

$$\frac{1}{2}(|\hat{u}|^2 + |\hat{v}|^2) = \frac{1}{2}\left(\frac{|\hat{\zeta}|^2}{K^2} + \frac{|\hat{\delta}|^2}{K^2}\right), \tag{2.36}$$

where $\hat{\zeta} = ik\hat{v} - il\hat{u}$ and $\hat{\delta} = ik\hat{u} + il\hat{v}$ are the horizontal Fourier coefficients of the vertical vorticity and horizontal divergence, respectively. Therefore, using equation (2.35), we can write the energy in the shell, $S_{K'}$, as

$$E(K')\Delta K \approx \sum_{\boldsymbol{k}\in S_{K'}} \frac{1}{2}\left(\frac{|\hat{\zeta}|^2}{K^2} + \frac{|\hat{\delta}|^2}{K^2}\right). \tag{2.37}$$

A similar process to the above described binning can also be done to find the contribution of rotational and divergent motion for wavenumbers in $(K' - \Delta K/2, K' + \Delta K/2)$.

This decomposition is useful in that the divergent part of the energy spectrum is an indication of gravity waves. In fact, it is trivial to note that QG and SQG have zero horizontal divergence at leading order. On the other hand, gravity waves do have horizontal divergence. This is most readily seen by using the incompressibility condition, $\nabla_H \cdot \boldsymbol{u} = -\partial_z w$. Using the results in section 1.1.4, for a single Fourier mode, we have,

$$\nabla_H \cdot \boldsymbol{u} = -\frac{\partial w}{\partial z} = \Re\{-m\cos(mz)\hat{w}e^{i(kx+ly-\omega t)}\}, \tag{2.38}$$

in general the above equation will not be zero. Thus, we see that gravity waves have non-zero divergent energy.

2.2.3 Energy Spectrum of the Surface Quasi-Geostrophic Model

In Kolmogorov 1941 [26] it is shown that the energy spectrum for three-dimensional isotropic turbulence followed a $K^{-5/3}$ power law. This result was very important and was based entirely on dimensional analysis of the governing equations of motion. For QG turbulence a similar results exists and was described by Charney 1971 [9]. Charney's theory

predicted a power law of K^{-3}. For SQG, however, the predicted power law is not -3. In Pierrehumbert et al. 1994 [37] the spectra of different types of two-dimensional turbulence are discussed from a mathematical perspective. In particular, they consider the general equation

$$\frac{\partial q}{\partial t} + J(\psi, q) = 0, \tag{2.39}$$

with an inversion relation of the form

$$\hat{q} = -K^{\alpha}\hat{\psi}, \tag{2.40}$$

where $\alpha \in [0, \infty)$. Note that only $\alpha = 1, 2$ are physically realizable. The case with $\alpha = 2$ corresponds to two-dimensional dynamics described by the Euler equations (i.e. conservation of vorticity [27]) while $\alpha = 1$ corresponds to the SQG model in Held et al. 1995 [19] (see also section 1.1.3). Pierrehumbert et al. 1994 [37] confirmed that the case with $\alpha = 2$ yields the classical K^{-3} energy spectrum for the down-scale enstrophy cascade and showed that SQG turbulence, the case when $\alpha = 1$, has an energy spectrum of $K^{-5/3}$ for the down-scale energy cascade. While SQG turbulence is two-dimensional, the predicted power law is different from that of the two-dimensional Euler equations.

Here, we present the basic outline of the scale analysis that is used in Pierrehumbert et al. 1994 [37] to show that SQG turbulence has a power law of $K^{-5/3}$. First, suppose we force the system at small wavenumber, k_i, and viscous dissipation occurs at large wavenumber, k_d. For wavenumbers satisfying, $k_i \ll k \ll k_d$, the dynamics do not directly feel the input of energy into the system nor the viscous dissipation of energy in the system. This set of wavenumbers is known as the inertial range (e.g. [11], [33]). Furthermore, it can be shown (e.g. [11], [33]) that, in the inertial range, the energy spectrum obeys,

$$\frac{\partial E(K,t)}{\partial t} = T(K,t), \tag{2.41}$$

where $T(K,t)$ represents non-linear transfer of energy between length scales (e.g. [11], [33]). The spectral flux is defined as

$$\Pi(K,t) = -\int_0^K T(K',t)dK', \tag{2.42}$$

which implies that equation (2.41) can be equivalently written as

$$\frac{\partial E}{\partial t} = -\frac{\partial \Pi}{\partial K}. \tag{2.43}$$

A fundamental assumption is that in the inertial subrange we have statistical stationarity, $dE/dt = T(K,t) = 0$ (e.g. [33], [37]). This means that $\Pi(K,t) = \epsilon$, where ϵ is a constant. From here, one can turn to dimensional analysis. Since we assume we are in the inertial range, the only relevant variables that describe the system are $\Pi, E(K), K$. Dimensionally, we have,

$$[\Pi] = L^2T^{-3}, \quad [E(K)] = L^3T^{-2}, \quad [K] = L^{-1}. \tag{2.44}$$

In order to see how Π relates to the other two variables dimensionally, set,

$$[\Pi] = [E(K)]^{\alpha}[K]^{\beta}. \tag{2.45}$$

After substituting in the dimensions in (2.44), we have,

$$L^2T^{-3} = L^{3\alpha}T^{-2\alpha}L^{-\beta}. \tag{2.46}$$

By equating exponents on the length and time scales, we find that $\alpha = 3/2$ and $\beta = 5/2$. This means that the energy spectrum has the form,

$$E(K) = \epsilon^{2/3}K^{-5/3}. \tag{2.47}$$

Therefore, as in Pierrehumbert et al. 1994 [37], we find that the predicted power law of the energy spectrum for turbulent flows in the SQG model is $K^{-5/3}$.

2.3 The ω Equation

The ω equation describes that vertical velocity that is induced by QG motion [20]. The nomenclature comes from meteorology. In meteorology, it is common use pressure, p, as the vertical coordinate (e.g. [16], [46]). As a result, the vertical velocity is defined (e.g. [16], [46]) as,

$$\omega = \frac{Dp}{Dt}. \tag{2.48}$$

However, in Hoskins et al. 1978 [20] the vertical coordinate remains written as height, z, and, therefore, we do not have to worry about writing things in pressure coordinates. The ω equation will become a useful diagnostic in that it will allow us to differentiate between gravity waves that are generated in our simulations from the vertical velocity due to the balanced motion. This technique is commonly used (e.g. [10]) to identify gravity waves. In this section, we shall give a brief derivation of the ω equation and discuss how we solve it numerically.

2.3.1 Derivation of the ω Equation

Preliminary Equations

We first note that the velocity field be written, in dimensional variables, as,

$$\boldsymbol{v} = \boldsymbol{v_g} + \boldsymbol{v_{ag}}, \tag{2.49}$$

where $\boldsymbol{v_g}$ is the geostrophically balanced horizontal velocity defined in (1.41) with vertical component identically zero (see section 1.1.3) and $\boldsymbol{v_{ag}}$ the ageostrophic velocity. When the Rossby number is small, we assume that $|\boldsymbol{v_g}| \gg |\boldsymbol{v_{ag}}|$.

If we consider the horizontal momentum equation,

$$\frac{D\boldsymbol{u}}{Dt} + \boldsymbol{f} \times \boldsymbol{u} = -\frac{1}{\rho_0}\nabla_H p, \tag{2.50}$$

one can show, using,

$$\boldsymbol{f} \times \boldsymbol{u} = \boldsymbol{f} \times \boldsymbol{u_{ag}} + \boldsymbol{f} \times \boldsymbol{u_g} = \boldsymbol{f} \times \boldsymbol{u_{ag}} - 1/\rho_0 \nabla_H p, \tag{2.51}$$

that the geostrophic momentum equation (e.g. [16]) can be written as,

$$\frac{D_g \boldsymbol{u}_g}{Dt} + \boldsymbol{f} \times \boldsymbol{u_{ag}} = 0, \tag{2.52}$$

or, in component form,

$$\frac{\partial u_g}{\partial t} + \boldsymbol{u_g} \cdot \nabla_H u_g - f v_{ag} = 0, \tag{2.53}$$

$$\frac{\partial v_g}{\partial t} + \boldsymbol{u_g} \cdot \nabla_H v_g + f u_{ag} = 0. \tag{2.54}$$

The other equation required for the derivation of the ω equation is the energy equation in (1.13). With $N = const$, we have,

$$\frac{\partial b'}{\partial t} + \boldsymbol{u_g} \cdot \nabla_H b' + N^2 w = 0. \tag{2.55}$$

Finally, we have thermal wind balance which we first stated, non-dimensionally, in (1.32). We state it here, dimensionally, as,

$$f\frac{\partial u_g}{\partial z} = -\frac{\partial b'}{\partial y}, \quad f\frac{\partial v_g}{\partial z} = \frac{\partial b'}{\partial x}. \tag{2.56}$$

Derivation

Our derivation of the ω equation follows Hoskins et al. 1978 [20]. To begin, first take an x derivative of (2.55),

$$\frac{\partial^2 b'}{\partial x \partial t} + N^2 \frac{\partial w}{\partial x} = -\frac{\partial}{\partial x}(\boldsymbol{u_g} \cdot \nabla_H b'). \tag{2.57}$$

Since we have thermal wind balance (2.56), we take a vertical derivative of (2.54) and multiply by f. Upon substitution into (2.57), we find,

$$N^2 \frac{\partial w}{\partial x} - f^2 \frac{\partial u_{ag}}{\partial z} = -\frac{\partial}{\partial x}(\boldsymbol{u_g} \cdot \nabla_H b') + f \frac{\partial}{\partial z}(\boldsymbol{u_g} \cdot \nabla_H v_g), \tag{2.58}$$

and, after some simplification which includes use of thermal wind balance (1.32) and incompressibility (1.7), we find,

$$N^2 \frac{\partial w}{\partial x} - f^2 \frac{\partial u_{ag}}{\partial z} = -2 \left(\frac{\partial b'}{\partial y} \frac{\partial v_g}{\partial x} - \frac{\partial b'}{\partial x} \frac{\partial v_g}{\partial y} \right) \equiv -2Q_1. \tag{2.59}$$

Similarly, we can take a y derivative of (2.55) and, using the same steps as described above, can find

$$N^2 \frac{\partial w}{\partial y} - f^2 \frac{\partial v_{ag}}{\partial z} = -2 \left(-\frac{\partial b'}{\partial y} \frac{\partial u_g}{\partial x} + \frac{\partial b'}{\partial x} \frac{\partial u_g}{\partial y} \right) \equiv -2Q_2. \tag{2.60}$$

Next, we take an x derivative of (2.59) and y derivative of (2.60) and add the resulting equations to find,

$$N^2 \nabla_H^2 w + f^2 \frac{\partial}{\partial z} \left(-\frac{\partial u_{ag}}{\partial x} - \frac{\partial v_{ag}}{\partial y} \right) = -2 \nabla_H \cdot \boldsymbol{Q}. \tag{2.61}$$

The last step is noting that the incompressibility condition of the ageostrophic velocity is written as,

$$\frac{\partial u_{ag}}{\partial x} + \frac{\partial v_{ag}}{\partial y} + \frac{\partial w}{\partial z} = 0. \tag{2.62}$$

Upon substituting into (2.61), we find the ω equation,

$$\left(N^2 \nabla_H^2 + f^2 \frac{\partial^2}{\partial z^2} \right) w = -2 \nabla_H \cdot \boldsymbol{Q}, \tag{2.63}$$

where $\boldsymbol{Q} = -(\nabla_H b'^{\perp} \cdot \nabla_H) \boldsymbol{u_g^{\perp}}$ and $\boldsymbol{u_g^{\perp}} = (-v_g, u_g)$ and $\nabla_H b'^{\perp} = (-\partial_y b', \partial_x b')$ (notation follows [49]). Note that the ω equation does not state how the balanced vertical velocity evolves in time. Thus, in order to find the field, we must compute the various terms in the equation and solve the differential equation for the balanced vertical velocity. This can be quite time consuming as will be described in the next section.

2.3.2 Computing the ω Equation in Practice

In order to compute the vertical velocity due to thermal wind and geostrophic balance, we write the ω equation (2.63), in spectral space, as,

$$\left(-N^2K^2 + f^2\frac{d^2}{dz^2}\right)\hat{w} = -2\widehat{\nabla\cdot\boldsymbol{Q}}. \tag{2.64}$$

The definition of the vector $\boldsymbol{Q}$ (defined in equations (2.59) and (2.60)) involves geostrophically balanced horizontal velocities and a buoyancy field which is in thermal wind balance. In order to compute the corresponding geostrophic velocities and thermal wind, we take derivatives of the pressure field, p,

$$v_g = \frac{1}{f\rho_0}\frac{\partial p'}{\partial x}, \quad u_g = -\frac{1}{f\rho_0}\frac{\partial p'}{\partial y}, \quad \text{and } b' = \frac{1}{\rho_0}\frac{\partial p'}{\partial z}. \tag{2.65}$$

All derivatives are computed uses the DFT. The vertical derivative of p is computed by performing an even extension of the pressure field and computing the derivative using DCT to transform into spectral space.

In equation (2.64), we approximate the second vertical derivative using a centered finite difference scheme. From there, we loop through all wavenumbers and invert the operator on the left hand side of (2.64) to find $\hat{w}(k,l,z)$ at each (k,l). Looping through each individual wavenumber takes a non-trivial amount of time, on the order of hours. The final step is to perform the inverse DFT to find the vertical velocity in physical space.

Chapter 3

Results

In this chapter we discuss and analyze the numerical solutions to the SQG and PE models. The SQG model assumes an infinitesimal Rossby number while in the PE the Rossby number is finite. The initial conditions we consider is that of an elliptical vortex which was the first example discussed by Held et al. 1995 [19]. The surface buoyancy anomaly field is given by an asymmetric Gaussian profile,

$$b^t = b_{\max} \exp\left(-\left(\frac{x}{l/6}\right)^2 - \left(\frac{4y}{l/6}\right)^2 \right), \tag{3.1}$$

where $b_{\max} = 0.01$ m s^{-2} and $l = 200$ km is the side length of horizontal domain. The three-dimensional buoyancy field is computed via (1.51) and the horizontal velocity fields are computed by taking horizontal derivatives of the three-dimensional streamfunction in (1.50). The vertical velocity field is initially zero everywhere. The initial surface buoyancy in equation (3.1) is shown in figure 3.1.

Our investigation is based on varying the Rossby number in the PE in order to determine when the SQG model breaks down for the elliptical vortex. While the choice of an isolated vortex is somewhat idealized, we felt it was a natural starting point in discussing SQG dynamics in the context varying Rossby number. In order to vary the Rossby number, Ro, we have a variety of choices. The most physical choice would be to vary the initial characteristic horizontal velocity, U, and leave all other parameters the same (i.e. fix $f = 10^{-4}$ s^{-1}, $L = 100$ km). However, the time-scale of the vortex, $T \sim L/U$, would be increased. In particular, using $L = 100$ km and $f = 10^{-4}$ s^{-1}, to get $Ro = 0.005$ (one of the cases we explore), the velocity would need to be $U = 0.05$ m s^{-1}. The corresponding time-scale is $T \sim O(10)$ days. Since, we've integrated our initial conditions for 20 times the

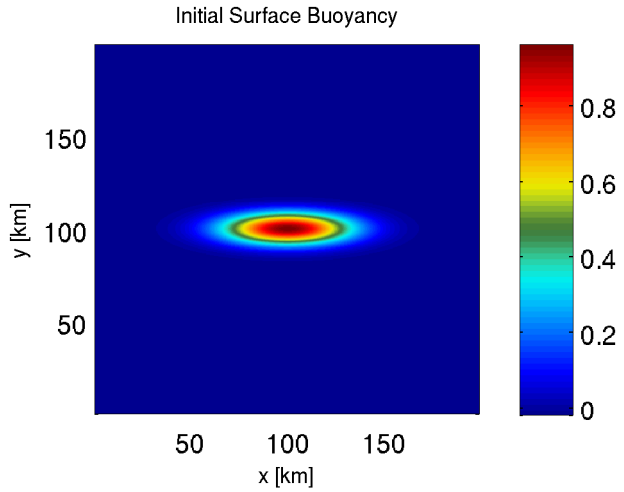

Figure 3.1: Initial surface buoyancy distribution. Surface buoyancy is normalized by b_{max}.

time-scale of the vortex (seen throughout this chapter), we would need to integrate up to at least 200 days with a fixed time-step of 60 seconds to ensure that the inertia-gravity waves are properly resolved (see section 1.1.4). This would require a huge amount of computing time. Therefore, the characteristic velocity and length scales are held fixed throughout the runs.

In order to vary the Rossby number, we choose to vary the Coriolis parameter, f. Since the time scale of the vortex is L/U but the time-step in SPINS is controlled by N, we find that by changing f we keep the time-scale of the vortex unchanged and, therefore, different Rossby number simulations can be run in about the same amount of time. However, varying f has the effect of changing the Burger number and, consequently, based on equations (1.50) and (1.51), the e-folding vertical scale of surface buoyancy features changes. Thus, in order to fix the Burger number, we can change either N or H. We choose to change H so that the decay per vertical grid point is the same between each case. Another way to think about this is that we change H to keep the depth of the domain relative to the depth of the vortex fixed. We note that by changing H the aspect ratio, H/L, between simulations changes but still remains much smaller than 1.

As discussed in section 2.1.5 we have two options in SPINS for the type of grid we can use in the vertical. The free-slip boundary condition permits the use of a uniform grid or Chebyshev grid. The uniform grid was first explored in this thesis but we note that, for computational reasons, this option forces a Neumann boundary condition at the vertical boundaries on the horizontal velocity fields and buoyancy field. This implies that the QG

PV, $q = \zeta + (f/N)^2\partial_z b'$, which is initially set to zero, will be spuriously generated near the surface due to the term $(f/N)^2\partial_z b'$ being forced to zero. The other option is to use the Chebyshev grid which has the advantage of high resolution near the surface where all of the dynamics are occurring. The disadvantage is the coarse resolution in the center which may filter out gravity waves propagating vertically. We first discuss the results of the Fourier simulations which use a uniform grid and then of the Chebyshev simulations.

3.1 Fourier Simulations

To begin, we consider simulations performed with a uniform vertical grid with cosine expansions for the horizontal velocities and buoyancy perturbations and sine expansions for the vertical velocity. This choice allows for uniform vertical resolution at the cost of imposing extra Neumann boundary conditions for the horizontal velocities, u, v, and buoyancy perturbations, b'. This will be compared with a Chebyshev grid in the vertical in section 3.2.

We consider cases for three different Rossby numbers that we classify based on the initial conditions. Table 3.1 shows the parameter values for the three PE runs. The characteristic velocity scale is chosen to be the maximum velocity induced by the surface buoyancy vortex (roughly, $U \approx 0.5$ m s^{-1}) while the characteristic length scale is chosen to be four times the standard deviation in the x-direction, $4\sigma \approx 95$ km, which we round up to 100 km.

Ro	f [s^{-1}]	H [km]	N [s^{-1}]	U [m s^{-1}]	L [km]	Δx [m]	Δz [m]	Δt [s]
0.005	10^{-3}	10	10^{-2}	0.5	100	390	20	60
0.05	10^{-4}	1	10^{-2}	0.5	100	390	2	60
0.1	$5 \cdot 10^{-5}$	0.5	10^{-2}	0.5	100	390	1	60

Table 3.1: The full set of parameter values for each run in the PE simulations.

The SQG solution is computed using the parameter values for the PE case with $Ro = 0.05$ in the QG3 solver (see section 2.1.4). Since SPINS uses a staggered grid where the grid points are at the center of the cell, in order to compare solutions at the same depth, we choose to project the SQG solution down half a grid point via equations (1.50) and (1.51). Even though the depth changes between PE simulations, the decay per grid point is identical. Throughout this section we often state that we are plotting fields at the surface. In actuality, we are plotting at $z = -\Delta z/2$ but we use the concise phrasing of "plotting at the surface."

For small scale dissipation, we use the exponential filter discussed in detail, including how it is applied in spectral space, in section 2.1.3. The parameter values for the PE simulations are given in table 3.2. For the SQG simulation, we use the same filtering parameters as the cases with $Ro = 0.005$ and 0.05. We note that for the case with $Ro = 0.1$ the filtering strength was increased. This was due to a build up of energy at small scales that was observed during the first few days of the simulation.

Ro	α	β	k_m	k_s
0.005	133.79	10.31	$0.4k_{\max}$	$0.5k_{\max}$
0.05	133.79	10.31	$0.4k_{\max}$	$0.5k_{\max}$
0.1	26.64	5.27	$0.35k_{\max}$	$0.5k_{\max}$

Table 3.2: Filter parameters used in our numerical simulations with SPINS.

3.1.1 Surface Buoyancy

As a natural starting point, we first consider how the surface buoyancy field evolves in time and space in both the SQG and PE models. Snapshots of the surface buoyancy at different times are plotted in figure 3.2 for the SQG solution. The vortex rotates anticyclonically and develops long thin filaments at the exterior of the vortex by the end of 5 days seen in panel (a). The thin filaments are unstable due to the strong shear that they possess and at around 10 days, instabilities can be observed. At $t = 15$ days we observe that the filaments break up and form coherent vortices. The simulation ends at 20 days, panel (d), and many small scale vortices have emerged. The evolution of the SQG vortex was first studied in Held et al. 1995 [19] and the instability mechanism has been studied in different contexts [19]. The generation of small scale vortices is a common feature of SQG dynamics, however, we note that the size of these secondary vortices are about 100 times smaller. This suggests that the Rossby number of these vortices may have increased (see section 3.1.4 for further discussion). This raises the question, do SQG dynamics apply to these small scale vortices and, if not, what dynamics are actually occurring? In order to begin addressing this, we turn to the PE.

Figure 3.3 shows the surface buoyancy at $t = 10$ days for the SQG model and the PE solutions corresponding to $Ro = 0.005, 0.05$, and 0.1 normalized by $b_{\max}$. As should be anticipated, the case with $Ro = 0.005$ matches closely to the SQG solution. There are some subtle differences between the two solutions. In particular, the thin filaments in the PE solution are slightly less sharp due to the vertical filtering that is present in SPINS

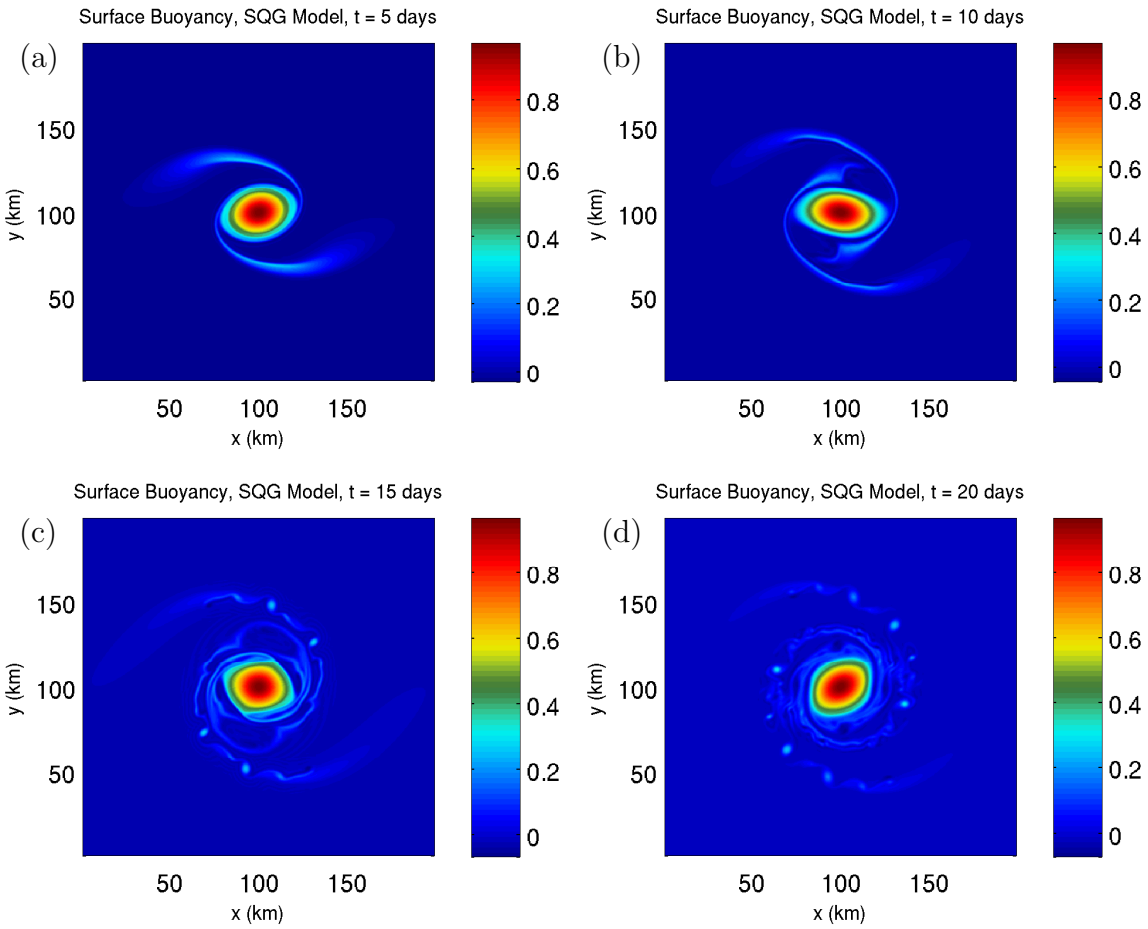

Figure 3.2: Surface buoyancy evolution at t =(a) 5, (b) 10, (c) 15 and (d) 20 days in the SQG model. Buoyancy fields are normalized by $b_{\max}$.

but not in QG3. Increasing the Rossby number ten-fold, we begin to notice stronger differences in the dynamics. Specifically, we see that the core of the vortex has expanded quite significantly and looks much more uniform. Furthermore, the maximum magnitude in the core has decreased from 1 to about 0.7. The thin filaments remain unstable and instabilities can be seen developing. In the PE solution with $Ro = 0.1$ we find that the dynamics have changed significantly. The core of the vortex has expanded out further and the maximum amplitude has decayed to around 0.4. The thin filament instabilities have vanished in this case.

Figure 3.4 shows the surface buoyancy field in the SQG model and the PE solutions at

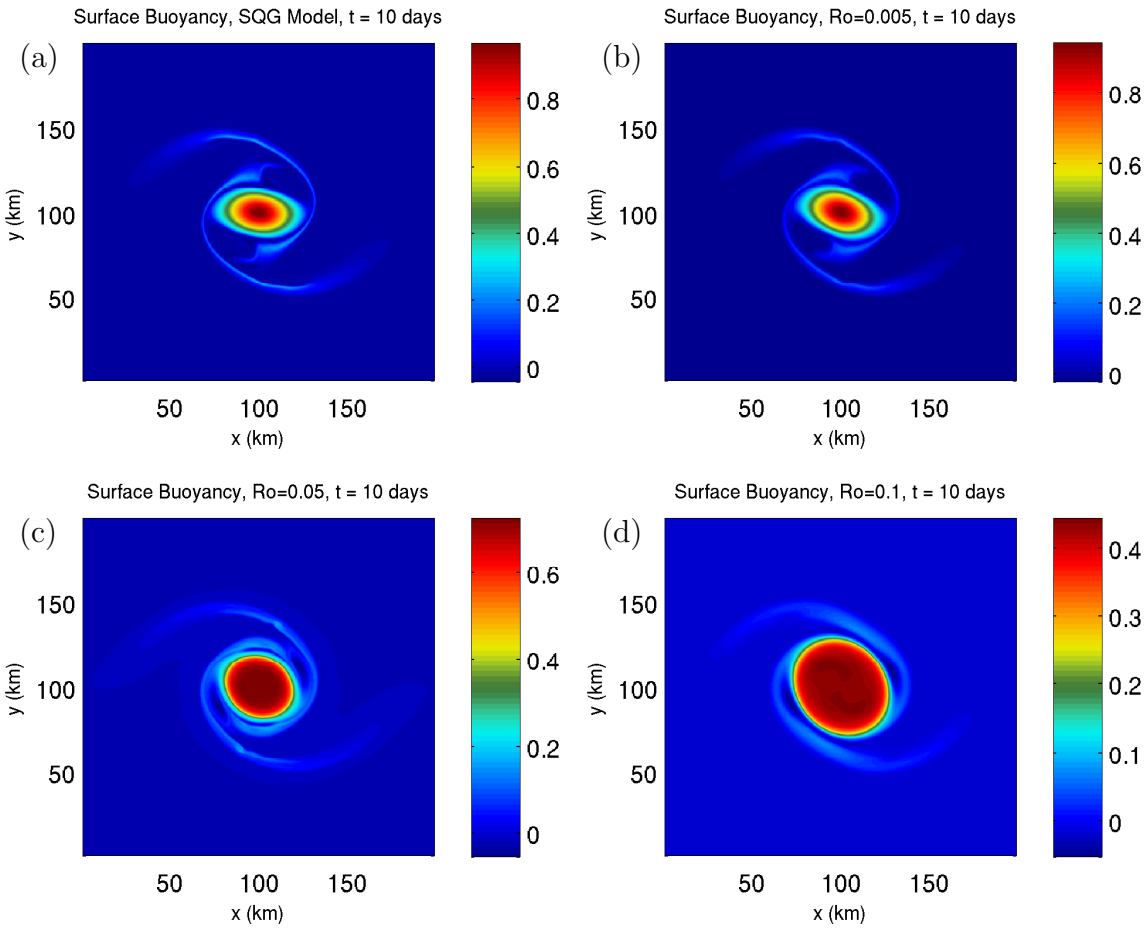

Figure 3.3: Surface buoyancy evolution at $t = 10$ days in (a) the SQG model and in the PE solutions with $Ro =$ (b) 0.005, (c) 0.05, and (d) 0.1. Buoyancy fields are normalized by $b_{\max}$.

$t = 20$ days. As is to be expected, the case with $Ro = 0.005$ looks remarkably similar to the SQG solution. The biggest difference is the decreased sharpness in the PE solution. The case with $Ro = 0.05$ departs quite dramatically from the SQG solution. In particular, no coherent secondary vortices have formed. This simulation was run for an additional 20 days and we observed that the instabilities were not able to form the secondary vortices seen in the SQG solution. Finally, the case with $Ro = 0.1$ shows a complete lack of instabilites on the filaments. Therefore, as the Rossby number increases, the thin filament instability common to SQG is stabilized. We note that while the increased filtering in the case with

$Ro = 0.1$ may explain the lack of instabilities present, the trend is quite clear between the cases with $Ro = 0.005$ and $Ro = 0.05$.

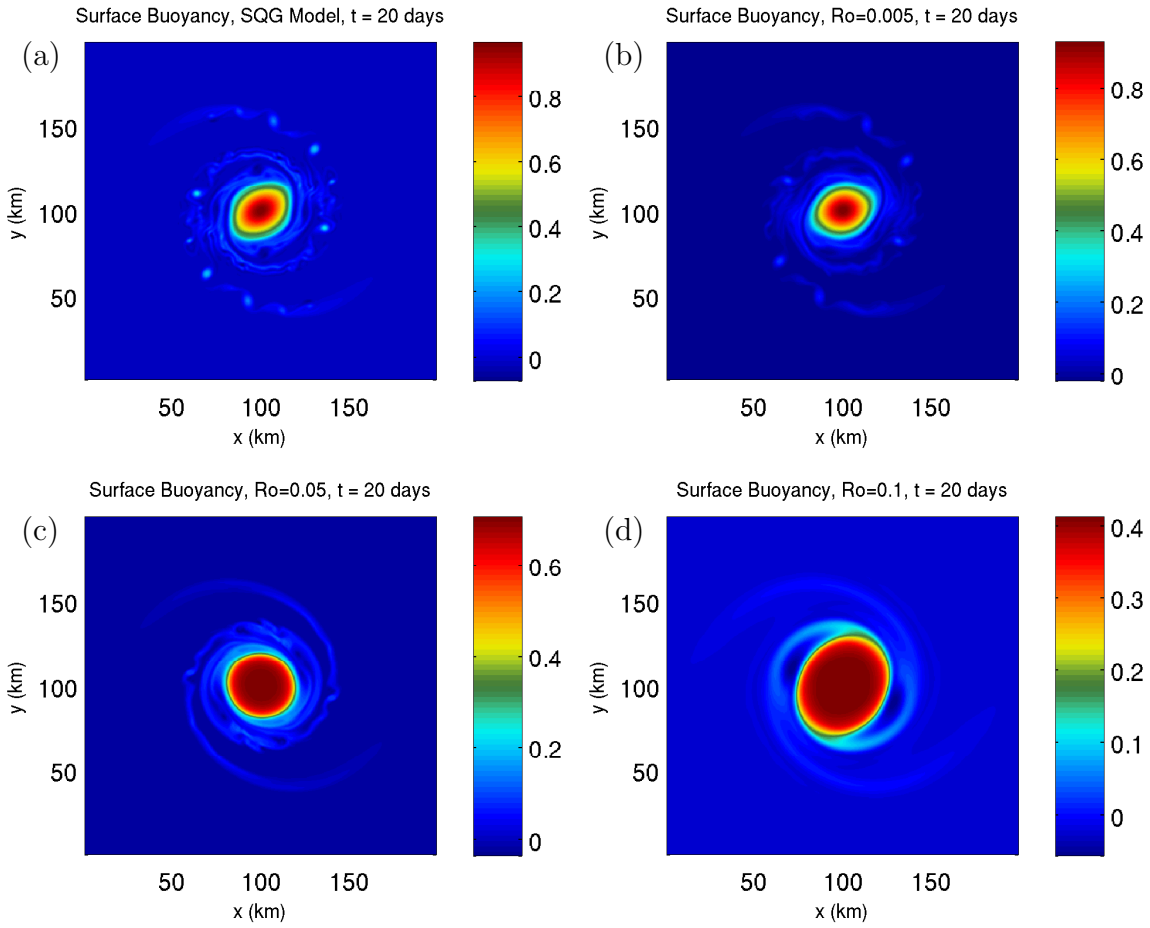

Figure 3.4: Surface buoyancy evolution at $t = 20$ days in (a) the SQG model and in the PE solutions with $Ro =$ (b) 0.005, (c) 0.05, and (d) 0.1. Buoyancy fields are normalized by $b_{\max}$.

3.1.2 Energy Spectra

In order to further diagnose the differences between SQG and the varying Rossby number solutions to the PE, we compute the time-averaged horizontal kinetic energy spectrum at

the surface of the fluid. We also compute the rotational and divergent parts of the energy spectrum in order to quantify how much divergent energy is growing as the Rossby number increases (recall that, at leading order, the horizontal velocity field in SQG is divergence free). The decomposition of horizontal kinetic energy into rotational and divergent parts give a rough look at the partition of kinetic energy between QG and inertia-gravity waves.

In figure 3.5 we show the time-averaged energy spectra over the mature part of the simulation between 15 - 20 days where each output is calculated over 12 hour intervals. As discussed in section 2.2.3, the energy spectrum in SQG turbulence is predicted to have a power law of $K^{-5/3}$ [37]. In panel (a), we see that the energy spectrum follows this power law quite closely. The PE solution with $Ro = 0.005$ matches quite closely with the SQG solution with some small-scale differences. The differences observed may be due to the fact that we have vertical dissipation in SPINS as well as the differences in how the filter is applied in QG3 and SPINS (see 2.1.3 for more details). The close agreement of the PE solution with $Ro = 0.005$ and SQG is to be expected since we have already seen remarkable agreement between these two cases in the snapshots of the surface buoyancy evolution. We also note that, while there is some divergent energy present, it is approximately 4 orders of magnitude smaller that the rotational energy. In the case with $Ro = 0.05$, the horizontal kinetic energy spectrum looks more closely to follow a -3 spectrum rather than a $-5/3$. Finally, the case with $Ro = 0.1$, again steepens to a spectrum closer to -3. The divergent part of the energy grows as the Rossby number increases. This is consistent with more energetic inertia-gravity waves being generated for larger Rossby numbers.

In table 3.3 we compute the least squares linear fit to the horizontal kinetic energy, rotational kinetic energy, and divergent kinetic energy spectra (log-log) for the SQG and PE solutions. In the SQG solution and PE solutions corresponding to $Ro = 0.005$ and 0.05 we compute the linear fit over wavenumbers 10-60 while in the case with $Ro = 0.1$, due to the increased strength of the filtering, we compute the fit over wavenumbers 10-30. The gradual increase in spectral slope indicates that the SQG model is not a very good fit to the PE solution when $Ro \geq 0.05$ and perhaps even for smaller values of Ro.

Based on equations (1.50) and (1.51) we see that features decays quite quickly away from the surface. In figure 3.6, we plot the energy spectra at $z/H \approx -0.1$ i.e. 10% below the surface (recall that the domain depth changes between simulations, see section 3.1 and table 3.1). Despite being only 10% below the surface, we find that the energy at the small scales has decayed significantly (2-3 orders of magnitude compared to that of the surface). The energy in the large scale vortex is still present and has not decayed significantly (seen here in small K). We also note that in the cases with $Ro = 0.05$ and $Ro = 0.1$ divergent energy begins to dominate the rotational energy at small scales. Furthermore, it is clear that smaller scale features are decaying in depth more slowly in the cases with $Ro = 0.05$

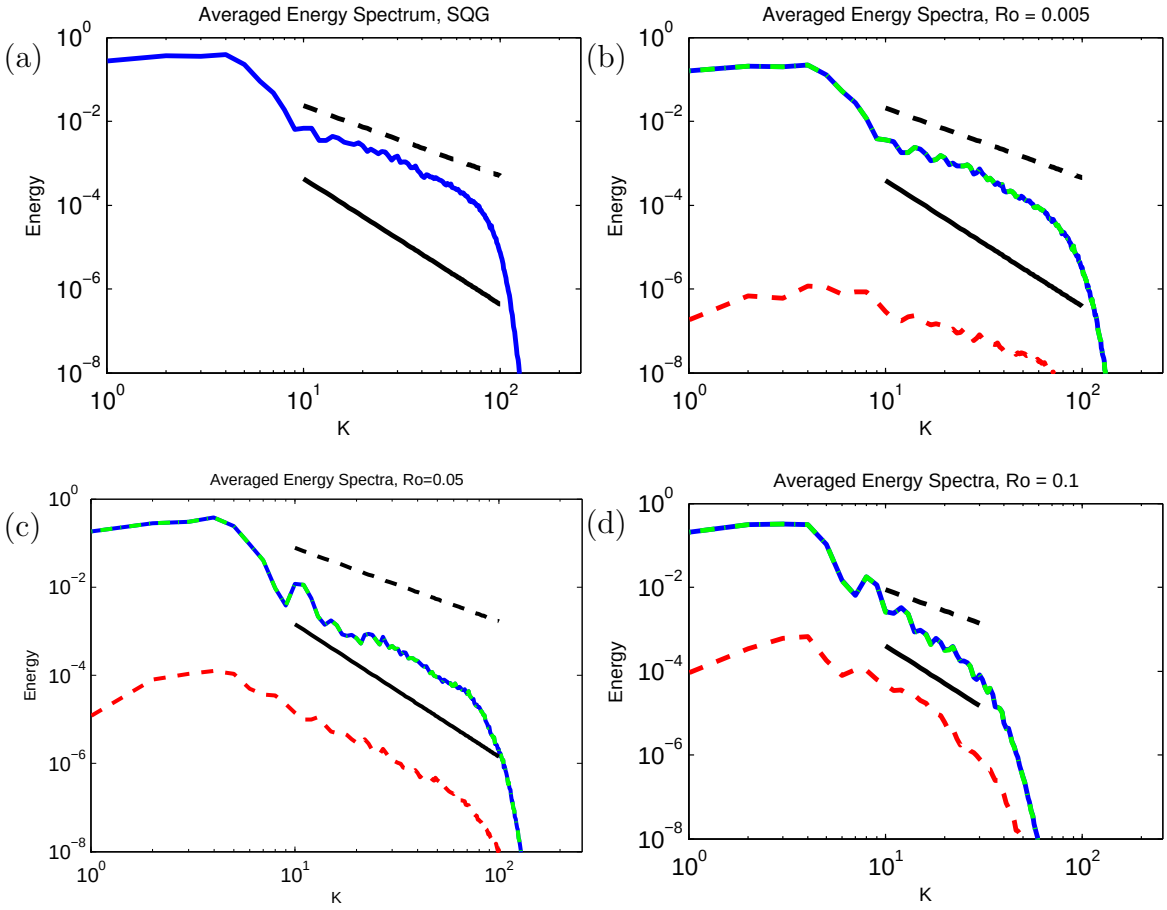

Figure 3.5: Energy spectrum in (a) the SQG model and the PE solutions with $Ro =$ (b) 0.005, (c) 0.05, and (d) 0.1. Energy has been normalized by the total initial horizontal kinetic energy and has been time-averaged over $t = 15 - 20$ days. The solid blue line corresponds to horizontal kinetic energy, while the green dash-dot line and red dash line correspond to rotational and divergent energy spectra, respectively. References line of powers laws pertaining to $-5/3$ and -3 are plotted in the dash black line and solid black line, respectively.

and $Ro = 0.1$ than in the case with $Ro = 0.005$.

In order to describe how the vertical distribution of energy changes we compute the ratio of divergent energy to rotational energy. Figure 3.7 shows the logarithm of the ratios of divergent to rotational energy time-averaged over $t = 15 - 20$ days. In all three PE

	KE	RKE	DKE
SQG	-1.91	-	-
$Ro = 0.005$	-2.12	-2.12	-1.55
$Ro = 0.05$	-2.56	-2.56	-2.37
$Ro = 0.1$	-3.51	-4.00	-3.50

Table 3.3: Least-squares estimate of spectral slopes of horizontal kinetic energy (KE), rotational kinetic energy (RKE), and divergent kinetic energy (DKE) for SQG solution and PE solutions.

solutions, we find that the divergent energy below a certain depth dominates rotational energy for most wavenumbers. This is not surprising since the gravity waves are able to propagate vertically while the rotating vortex is trapped near the surface. Perhaps unsurprisingly, the case with $Ro = 0.005$ (which had very little divergent energy) shows that rotational energy dominates for more of the vertical domain compared to the cases with $Ro = 0.05$ and 0.1.

3.1.3 Vertical Velocity and the ω Equation

The energy spectra in figures 3.5 and 3.7 showed a gradual increase of divergent energy as the Rossby number increased. This suggest that gravity waves are being generated in the PE simulations and should be identifiable in the vertical velocity field. In order to properly classify these waves we must compare the full velocity field to the vertical velocity field that is generated from geostrophically balanced motion. The vertical velocity due to the balanced part of the motion can be computed using the ω equation [20] (see section 2.3.1 for a derivation).

Figure 3.8 shows the full vertical velocity (left panels) and the ω equation velocity (right panels) computed at $t = 5$ days. The ω equation velocity is computed at $z = -\Delta z$ while the full vertical velocity is plotted at $z = -\Delta z/2$. Since we are simply trying to discern whether or not we have gravity waves in our simulation, we only consider the qualitative features in the velocity fields and, therefore, we argue that the discrepancy between plotting depths should not be too much cause for concern. In the case with $Ro = 0.005$, both velocity fields look similar. This suggests that the vertical velocity is dominated by the balanced part of the flow and not gravity waves. This is in agreement with the minimal divergent energy computed in the energy spectrum plot for the case with $Ro = 0.005$ in figure 3.5. On the other hand, both cases with $Ro = 0.05$ and 0.1 do generate gravity waves which are seen radiating away from the vortex. We note that in the case with $Ro = 0.1$, the wavelength

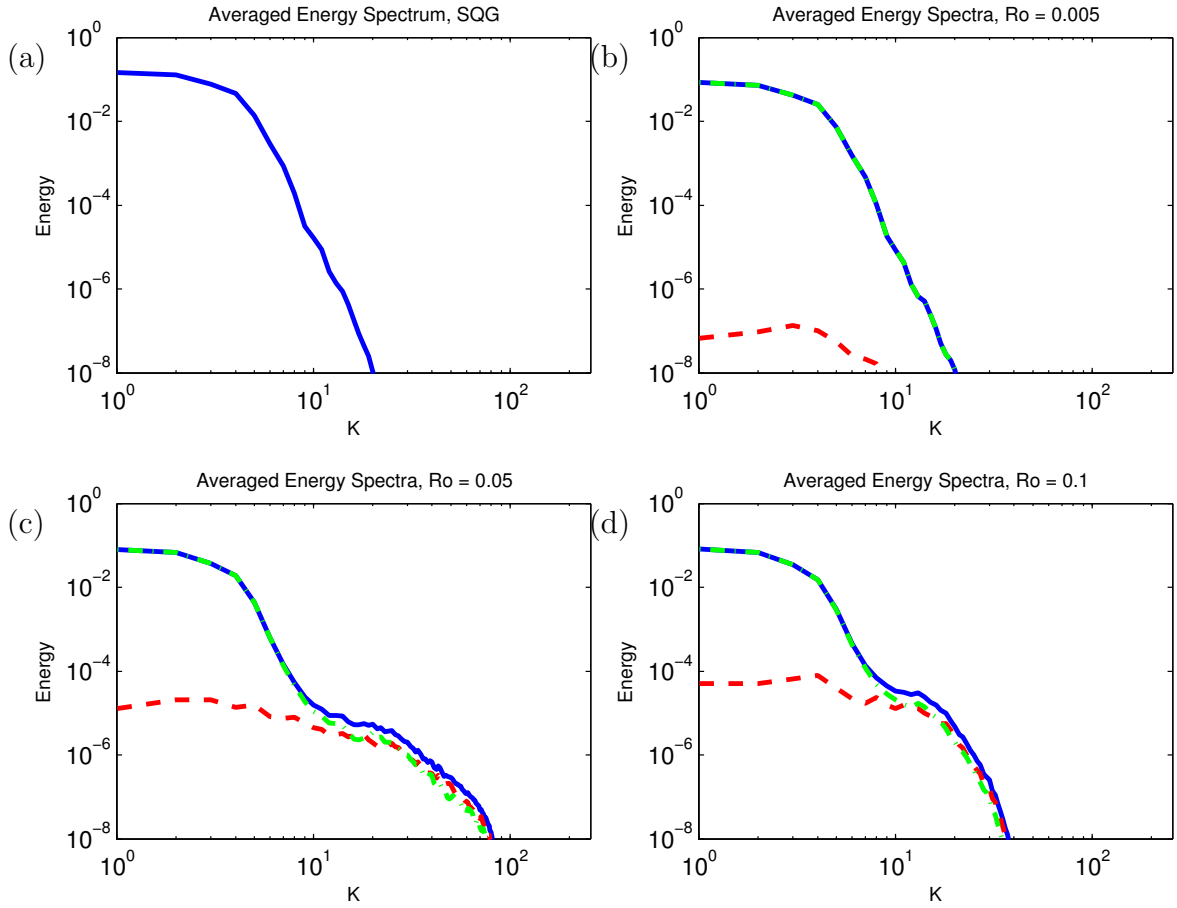

Figure 3.6: Energy spectra in (a) the SQG solution and the PE solutions with $Ro =$ (b) 0.005, (c) 0.05, and (d) 0.1. Energy spectra have been normalized by initial energy at the surface and wave number has been normalized by $2\pi/L$. These plots are plotted at $z/H \approx -0.1$.

of gravity waves has increased. A separate case of $Ro = 0.05$ with identical filtering as the case with $Ro = 0.1$ (not shown) indicates that the wavelength of gravity waves is set by the filtering strength. This suggests that we are not resolving the smallest wavelength gravity waves and it is therefore possible that gravity waves with smaller wavelength would be generated with increased resolution simulations.

In figure 3.9 we plot a vertical slice in the xz plane of the vertical velocity (left panels) and ω equation velocity (right panels) in the PE solutions. Common to all PE solutions is

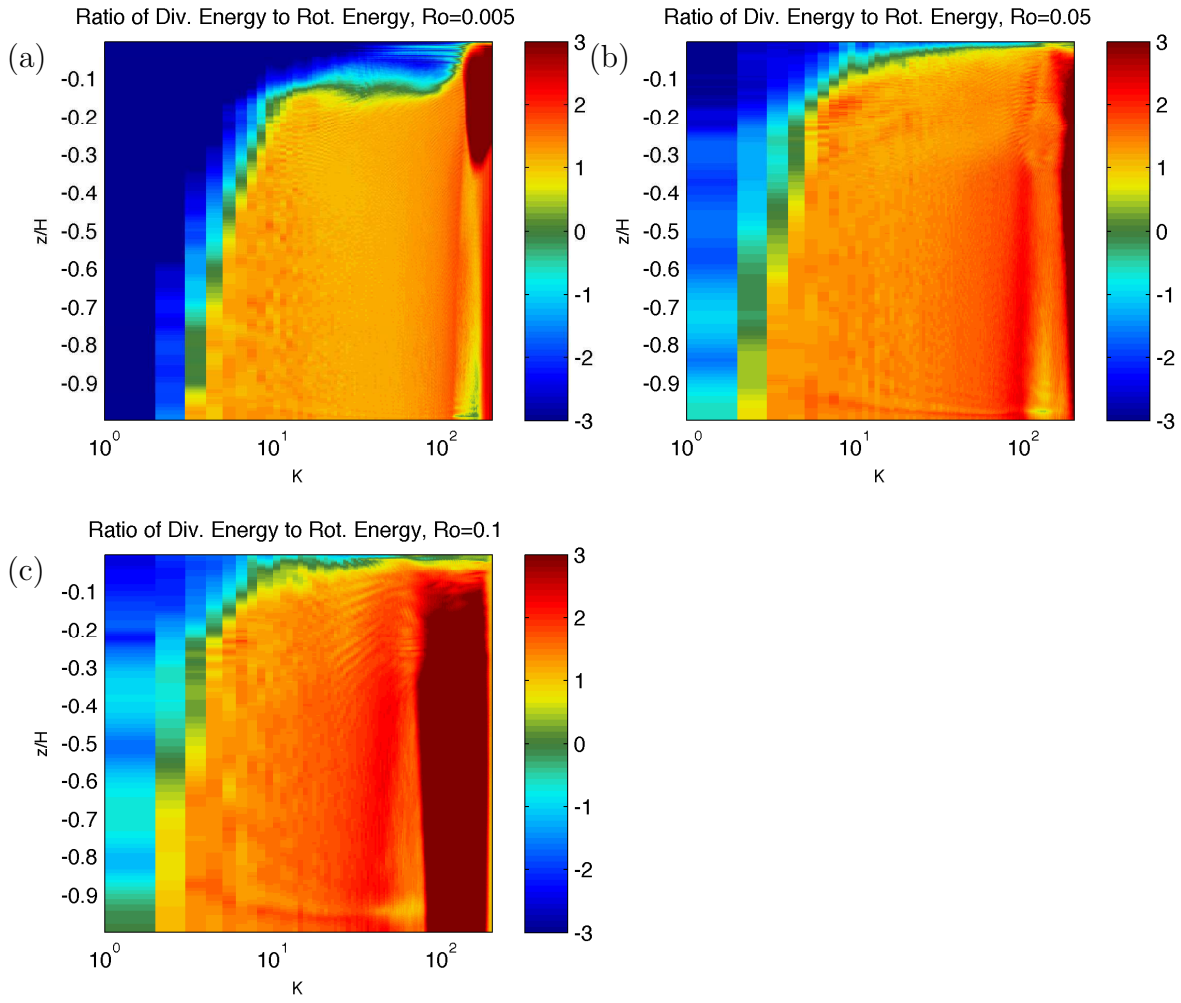

Figure 3.7: Logarithm of the ratio of divergent to rotational energy in the PE solutions with $Ro =$ (a) 0.005, (b) 0.05, and (c) 0.1.

the abundance of gravity waves propogating vertically (most readily seen in animations). The ω-equation velocities show that the geostrophically balanced vertical motion is always trapped near the surface, although, as the Rossby number increases we see that the geostrophically balanced velocities penetrate deeper into the fluid. The effect of the increased filtering is quite clear between the case with $Ro = 0.05$ and $Ro = 0.1$ in that we see larger wavelength waves in the case with $Ro = 0.1$.

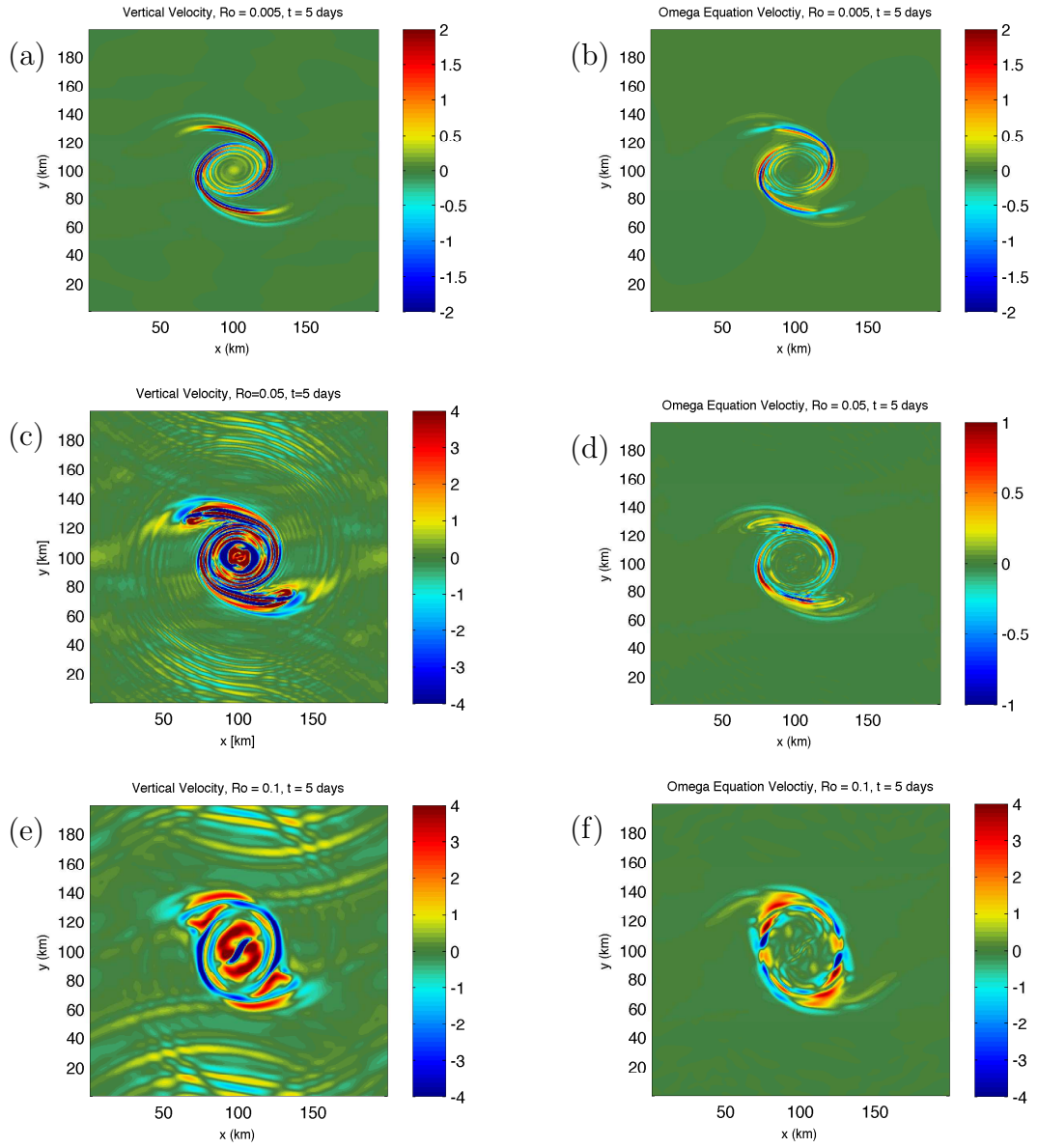

Figure 3.8: Vertical velocities (left panels) and vertical velocity induced by QG motion (right panels) for the set of Rossby number. Velocities are normalized by 10^{-5}.

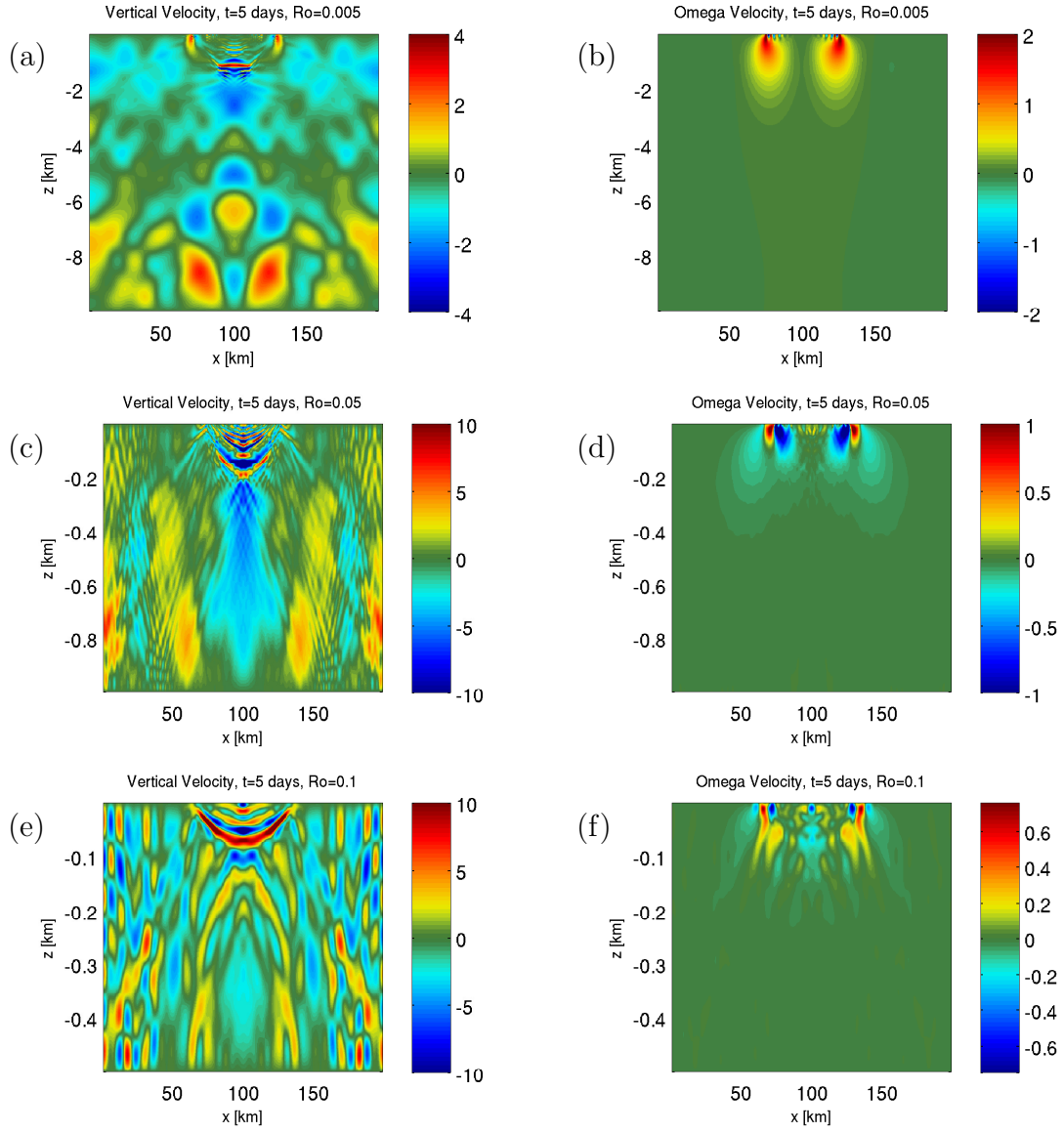

Figure 3.9: Cross section of vertical velocity (left panels) and ω velocities (right panels) in the PE solutions. Velocity has been normalized by 10^{-5}

3.1.4 Vertical Vorticity and the Local Rossby Number

While we use a definition of the Rossby number based on the initial conditions to classify each of the three cases, there are other ways to estimate the relative strength of advection

to rotation. In particular, one can define a local Rossby number by,

$$Ro_{loc} = \frac{\zeta}{f}, \tag{3.2}$$

where ζ is the vertical vorticity. The advantage of Ro_{loc} is that it reveals how relevant rotation is in different parts of the flow. In figure 3.10 we show the local Rossby number at the initial state of the flow for the case with $Ro = 0.05$. Initially, we have a strong anticyclone in the center which has two relatively weaker cyclones above and below the core anticyclone. The other cases have identical structures but with varying extrema due to the varying f values between cases. The extrema are

$$Ro = 0.005 : Ro_{loc} \in (-0.14, 0.02) \tag{3.3}$$
$$Ro = 0.05 : Ro_{loc} \in (-1.4, 0.2) \tag{3.4}$$
$$Ro = 0.1 : Ro_{loc} \in (-2.5, 0.5) \tag{3.5}$$

The local Rossby number is a stronger indication of whether or not the the flow is QG, however, we choose to use the Rossby number based on the initial conditions as the way to differentiate between cases. Indeed, the case with $Ro = 0.005$ is the only case where $|Ro_{loc}| < 1$ and this is the case which very closely resembles what SQG theory predicts while the other two cases depart from the SQG solution.

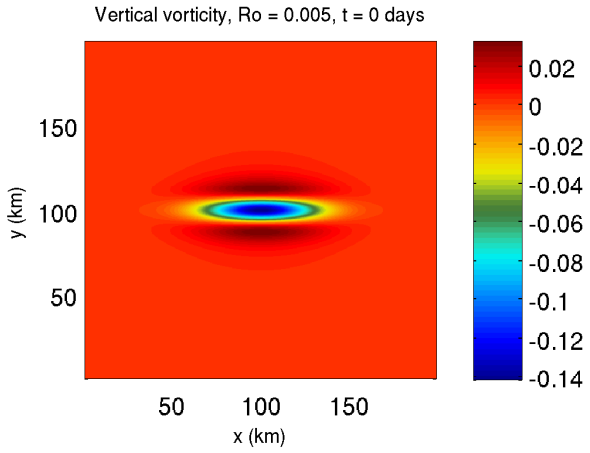

Figure 3.10: Vertical vorticity divided by f in the PE case with $Ro = 0.005$ at $t = 0$) days.

Figure 3.11 shows the vertical vorticity normalized by f at $t = 3$ days in the PE solutions. Here, we notice that the case with $Ro = 0.05$ and 0.1 have local Rossby numbers

that are at least 1 while the case with $Ro = 0.005$ maintains $Ro_{loc} \sim \mathcal{O}(0.1)$. Danioux et al. 2012 [10] showed in their simulations that when $Ro_{loc} \sim \mathcal{O}(1)$, gravity waves were spontaneously generated. We similarly find this phenomenon in our simulations: the cases with $Ro = 0.05$ and 0.1 both generate gravity waves and have local Rossby numbers that are at least 1 but the case with $Ro = 0.005$ does not show any clear evidence of gravity wave generation. Further, we see that the initial local Rossby number in (3.3)-(3.5) can grow quite dramatically. In particular, the cases with $Ro = 0.05$ and 0.1 attain a maximum local Rossby number of ≈ 2.5 and ≈ 4, respectively. This suggests that the local Rossby number can grow quite dramatically in PE simulations.

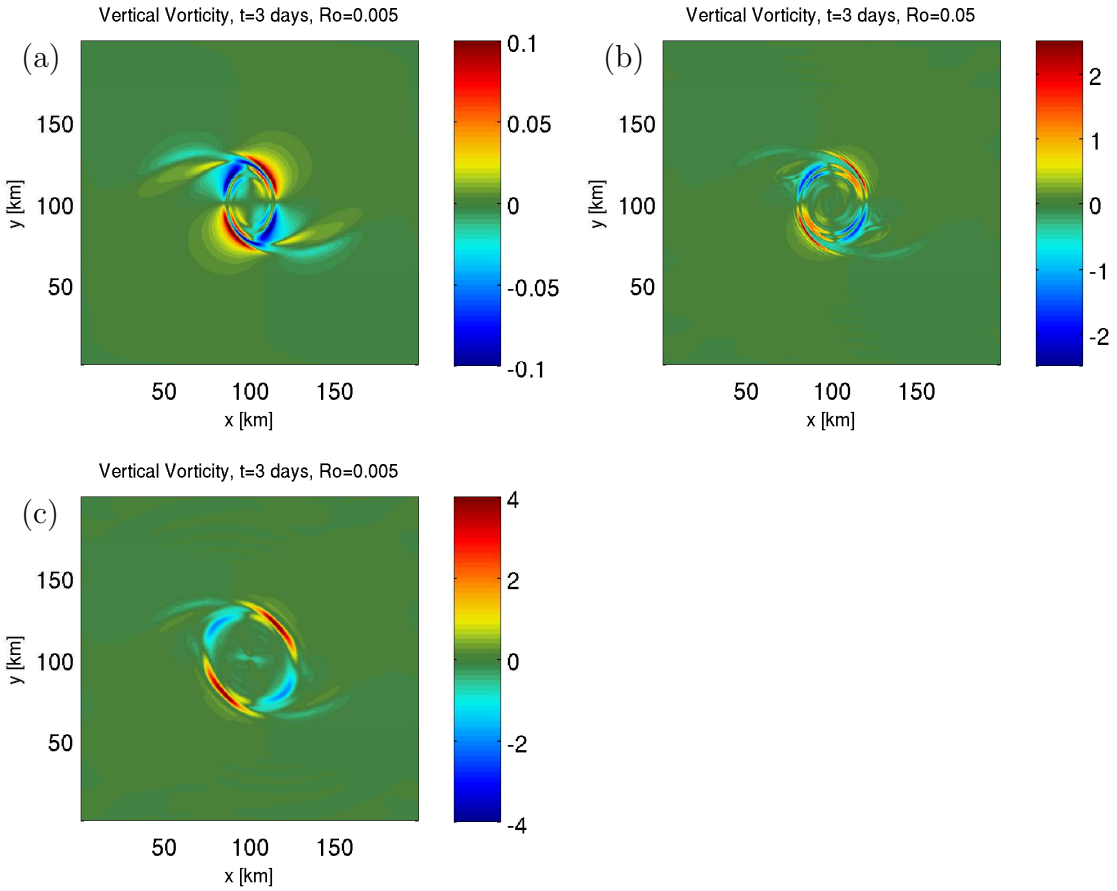

Figure 3.11: Vertical vorticity divided by f at $t = 3$ days in the PE model with $Ro =$ (a) 0.005, (b) 0.05, and (c) 0.1.

Looking further in the simulation, figure 3.12 shows plots of the local Rossby number

in the SQG solution along with the PE solutions with $Ro = 0.005, 0.05$, and 0.1 at $t = 15$ days. In the PE case with $Ro = 0.005$, all filaments and vortices remain $\mathcal{O}(0.1)$ and are therefore within the SQG regime. In the cases with $Ro = 0.05$ and 0.1 we find local Rossby numbers are $\mathcal{O}(1)$ which suggests that SQG should not be used to describe these dynamics. Indeed, simply based on the evolution of surface buoyancy one could deduce that these cases depart from SQG. Qualitatively, there is a weakening of vortex stretching as the Rossby number increases from 0.005 to 0.05 to 0.1 and this decreased shearing could be the reason for the stabilization of the thin filament instabilities seen in figures 3.2, 3.3 and 3.4. Finally, the SQG solution's local Rossby number shows $\mathcal{O}(1)$ structures and therefore, the initial vortex should not be evolved according to SQG dynamics.

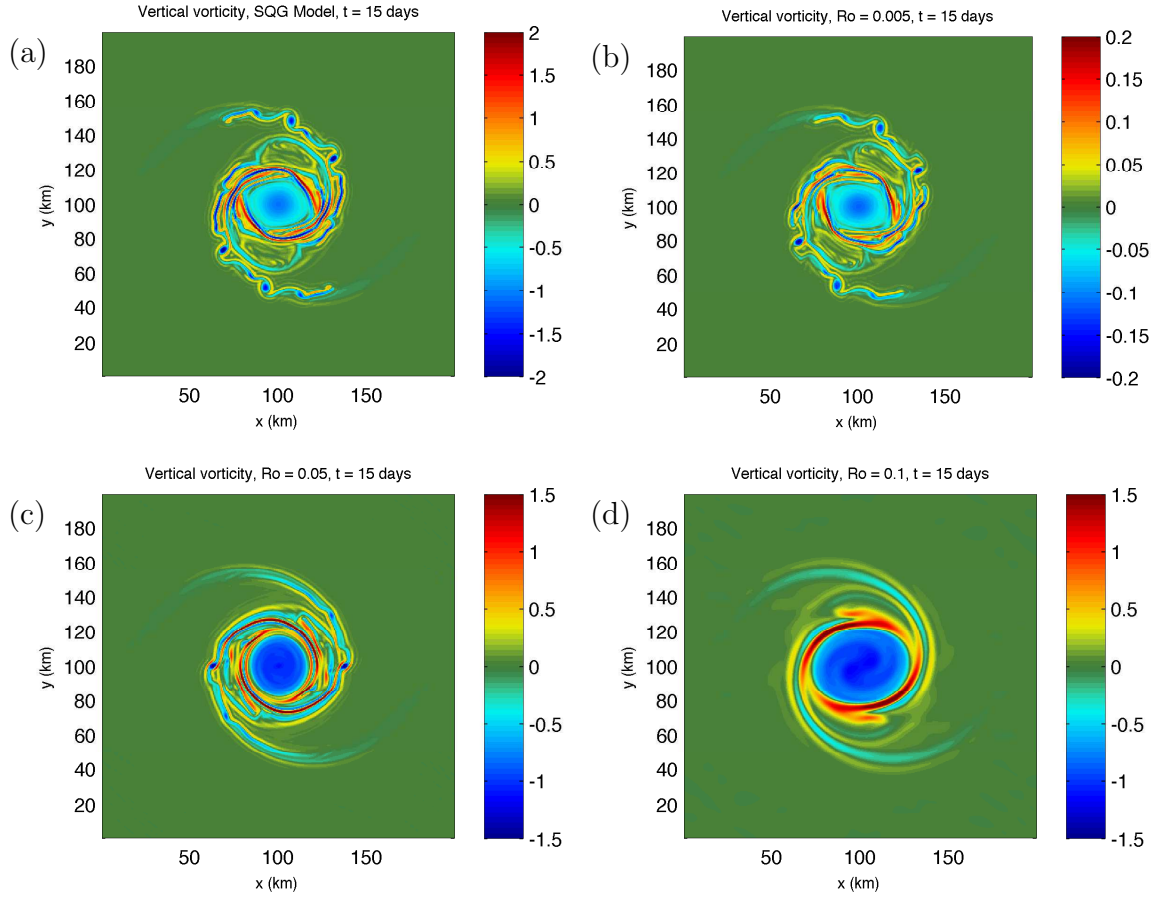

Figure 3.12: Vertical vorticity divided by f at $t = 15$ days in (a) the SQG model and in the PE model with $Ro =$ (b) 0.005, (c) 0.05, and (d) 0.1.

3.1.5 Quasi-Geostrophic Potential Vorticity

In the SQG model, since QG PV is materially conserved in the interior of the fluid and is initially set to zero, there can be no generation of QG PV. However, in the PE, QG PV is not necessarily materially conserved and therefore some generation through non-linear interactions is possible. In particular, in the PE, it is the Ertel PV that is materially conserved. QG PV is an approximation to the Ertel PV and is a good approximation when the Rossby number is small (i.e. when the relative strength of non-linear advection is weak to rotation). For a further discussion of Ertel PV see Vallis 2006 [46]). Due to the no mass flux condition at the top and bottom of the fluid, we find that QG PV is generated at $z = 0$ due to the enforced boundary condition. In figure 3.13 we plot $\zeta, (f/N^2)\partial_z b'$ and q in depth for the PE solution with $Ro = 0.005$ (since it matched closest with the SQG solution) at $t = 30$ minutes (the earliest output) and $t = 20$ days (the end of the simulation). The even extension of b' has a cusp and, therefore, the derivative is discontinuous. Using a Fourier basis results in Gibbs' oscillations near the point of discontinuity [42].

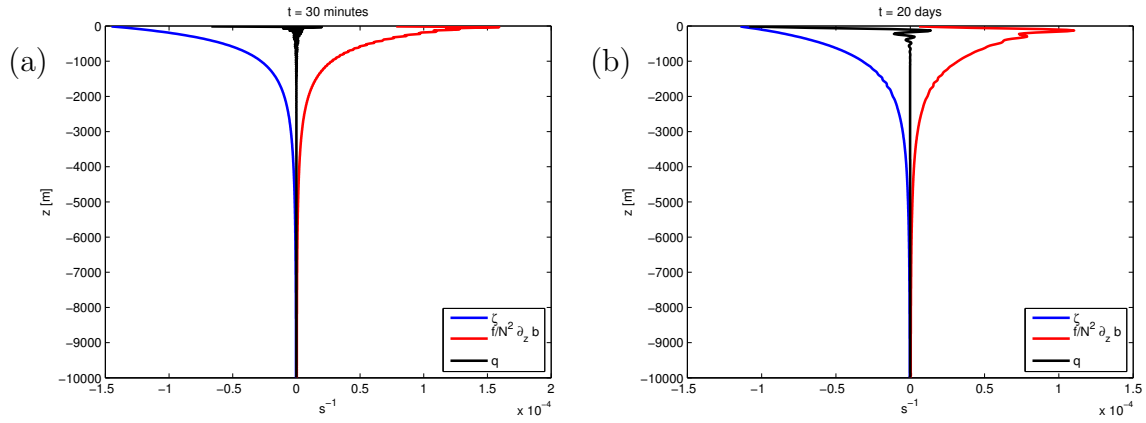

Figure 3.13: QG PV generation due to vertical boundary condition in the PE solution with $Ro = 0.005$ at (a) $t = 30$ minutes and (b) $t = 20$ days. Blue curve represents vertical vorticity, red curve represents $f/N^2\partial_z b'$, and black curve represents QGPV, q.

Far enough away from the surface, q is small compared to typical values of ζ but near the surface, where the no mass flux condition is enforced, we see generation of q. At $t = 20$ days, the error is quite striking: $q = \zeta$ since $\partial_z b' = 0$. While we note that our results matched very well between SQG and the PE solution with $Ro = 0.005$, we find it necessary to understand what, if any, effect this discrepancy has on the underlying dynamics. In the next section, we present results using a Chebyshev grid which does not

enforce the Neumann condition on u, v, and b' at the vertical boundaries and compare the results to the Fourier simulations to draw some conclusion about how significant this discrepancy is.

3.2 Chebyshev Simulations

The spurious introduction of QG PV near the surface due to the Neumann boundary condition on b' may affect the underlying dynamics in the Fourier simulations. The error comes about as a result of computing vertical derivatives of u, v, w, and b' which only occurs during the vertical advection step. As seen in section 3.1.3, the vertical velocity is quite small and therefore it is possible that the error might remain small and the Fourier simulation results still sound.

To understand how the spurious generation of QG PV near the surface affects the Fourier simulations, a second set of simulations were run using a Chebyshev grid in SPINS. Furthermore, a resolution test of the Chebyshev simulations was also done. The number of vertical grid points in the two resolution tests were 64 and 128, which we refer to as Cheb64 and Cheb128. Both of these choices improved the resolution near the boundary.

We discuss only the cases with $Ro = 0.05$ and 0.1 since the case with $Ro = 0.005$ was virtually identically to that of the corresponding Fourier simulation. For the Chebyshev simulations, the cases with $Ro = 0.1$ used the same filter as cases with $Ro = 0.05$ and therefore we cannot directly compare this to the corresponding $Ro = 0.1$ Fourier simulation. We note that the lack of proper filtering can contaminate dynamics at the small scales due to the pile-up of energy. Therefore, we focus on discussing the case with $Ro = 0.05$ with minimal discussion of the $Ro = 0.1$ case.

Finally, due to the staggered grid in the Fourier simulations, the plots of surface dynamics were plotted at a depth of $z = -\Delta z/2$. For the Chebyshev grid simulations we try to plot close to that depth to allow for a fair comparison. The exact depths are shown in table 3.4 (recall that Δz changes between free-slip simulations due to the varying depth between simulations. See discussion in section 3.1).

Ro	Fourier simulation depth [m]	Chebyshev simulation depth [m]
0.005	-20	n/a
0.05	-2.0	-2.4
0.1	-0.98	-1.2

Table 3.4: Depths of surface plots in the Fourier and Chebyshev simulations

3.2.1 Surface Buoyancy

The surface buoyancy field evolution remains qualitatively similar between the Fourier, Cheb64, and Cheb128 simulations across the three Rossby number cases we have previously discussed: $Ro = 0.005, 0.05$, and 0.1. In figure 3.14 we present the surface buoyancy for the case with $Ro = 0.05$ at $t = 20$ days. Both buoyancy fields look very similar to the case with $Ro = 0.05$ in the Fourier simulations shown in figure 3.4. In particular, we see the same instabilities developing on the thin filaments and the lack of generation of the secondary vortices. The core of the vortex has expanded and become quite uniform with the maximum amplitude being around 0.7. These promising results suggest that the Neumann boundary condition in the Fourier simulations does not have a dramatic impact on how the surface buoyancy field is evolving. As well, the horizontal velocity fields match quite well to the corresponding Fourier simulations.

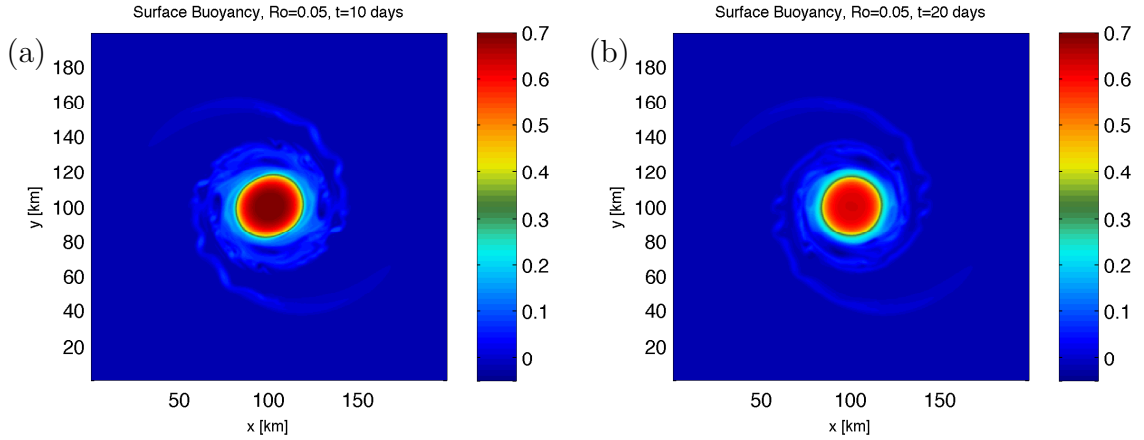

Figure 3.14: Surface buoyancy at $t = 20$ days in the Chebyshev simulations. Panel (a) has 64 vertical grid points while panel (b) has 128 vertical grid points. Surface buoyancy is normalized by $b_{\max}$.

3.2.2 Vertical Velocity

The major change that we find, perhaps unsurprisingly, is in the vertical velocity field. In figure 3.15 we plot the vertical velocity at the surface at $t = 5$ days for the cases with $Ro = 0.05$ and 0.1. The left panels show the vertical velocity in the Cheb64 simulations while the right panels show the vertical velocity for the Cheb128 simulations. The vertical

velocity in the cases with $Ro = 0.05$ are normalized by 10^{-6} while the velocity in the cases with $Ro = 0.1$ are normalized by 10^{-5}. An immediate difference between the Cheb64 and Cheb128 simulations in the case with $Ro = 0.05$ is that there is a larger abundance of waves present in the Cheb128 simulation. In fact, we see smaller wavelength waves present in the Cheb128. This result suggests that by increasing vertical resolution, we tend to resolve smaller horizontal scale features is discussed in Tulloch and Smith 2006 [44]. If we compare the vertical velocity in the Cheb128 simulation to its corresponding Fourier simulation shown in figure 3.8, we note there is an increased quantity of gravity waves being generated at surface. Since the Cheb128 simulation has better vertical resolution near the surface, this result could be explained by the discussion in Tulloch and Smith 2009 [44].

In the cases with $Ro = 0.1$ we do not see a difference in the amount of gravity waves which are generated nor the wavelength but there is quite a large difference in the dynamics of the core of the vortex. In particular, we notice that, similar to discussion between the Chebyshev cases with $Ro = 0.05$, there is a large abundance of small-scale features present in the core of the vortex in the Cheb128 simulation. Indeed, the Cheb128 simulation shows a complex picture of up-welling and down-welling in the core compared to the Cheb64 simulation. An interesting feature pertaining to the gravity waves in the cases with $Ro = 0.1$ is that the waves are farther apart, indicating that the waves may have been generated periodically during the first few days of the simulation. On the other hand, in the cases with $Ro = 0.05$, the waves are much closer together which suggest they are generated more frequently during the initial stages of the simulation. The free-slip case with $Ro = 0.1$ also shows evidence that gravity waves are periodically generated in the first few days of the simulation and also depicts a very smooth vortex core, however, the smoothness of the vortex core is likely due to the increased filter strength.

In figure 3.16 we show an xz cross-section of the vertical velocity of the Chebyshev cases with $Ro = 0.05$ through the center of the y axis. The increased resolution in the Cheb128 case demonstrates that the core of the vortex (trapped in the first ≈ 200 m) has a plethora of features. There is an alternating up-welling and down-welling pattern as we move down the core of the vortex that is not realized in the Cheb64 simulation. As well, we can see a large amount of gravity waves propagating in the Cheb128 run compared to the Cheb64 run. In the corresponding Fourier simulation case with $Ro = 0.05$ plotted in figure 3.9, we note that both Cheb64 and Cheb128 match the qualitative features of the free-slip simulation. However, near the surface of fluid, we find that Cheb64 does a poor job of matching the up-welling and down-welling pattern. The Cheb128 simulation matches the pattern much better and gives us confidence that the enforced Neumann vertical boundary condition in the Fourier simulations does not seem to be affecting the dynamics very much.

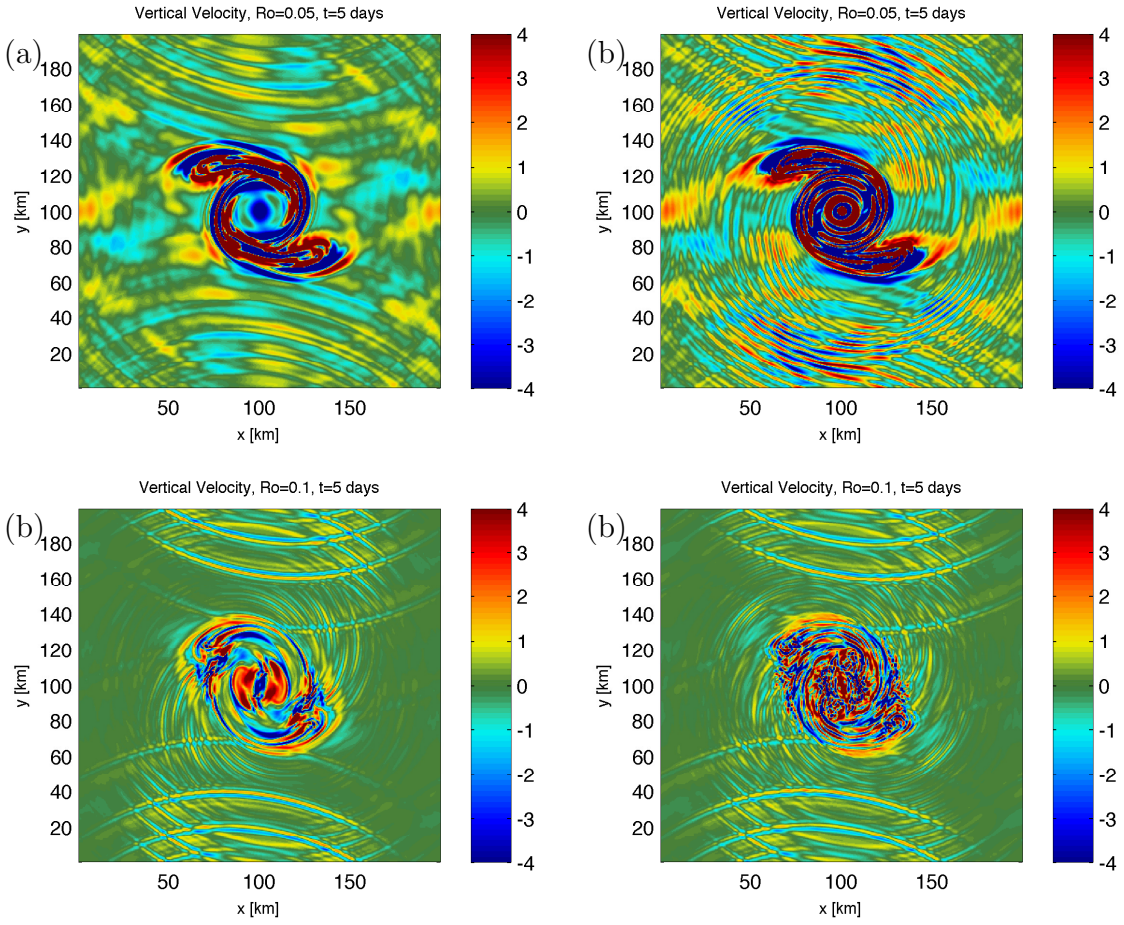

Figure 3.15: Vertical velocity near the surface in the Chebyshev simulations at $t = 5$ days. Panel (a) shows the simulation with 64 vertical grid points while panel (b) shows the simulation with 128 vertical grid points for the case with $Ro = 0.05$. Panel (c) and (d) show the case with $Ro = 0.1$ with 64 and 128 vertical grid points, respectively. Velocity is normalized by 10^{-6} in the cases with $Ro = 0.05$ and by 10^{-5} in the cases with $Ro = 0.1$.

However, one of the features that the Chebyshev simulation is unable to resolve is that propagation of small wavelength gravity waves that can be traced from the surface down to the bottom of the fluid and reflected back up in the corresponding Fourier simulation. Due to the relatively coarse resolution of the interior, small wavelength gravity waves are filtered out as they pass through this region.

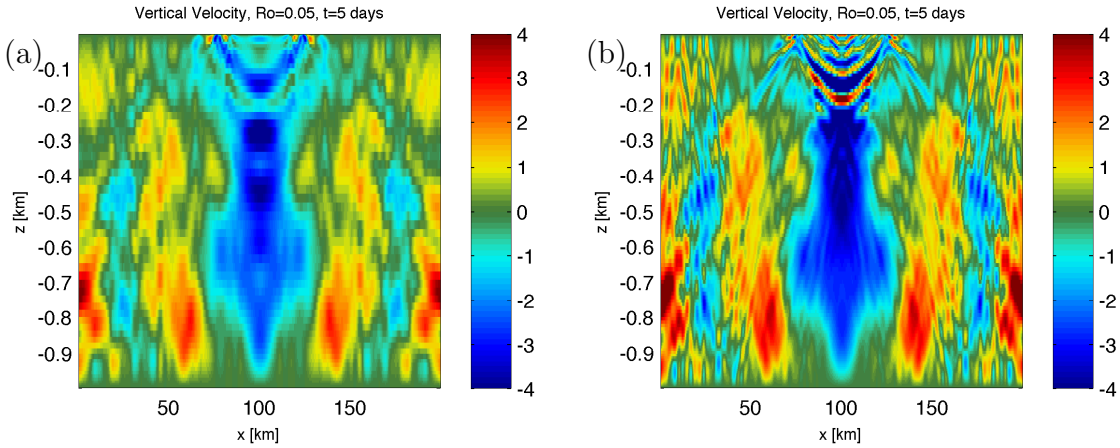

Figure 3.16: Vertical velocity cross-sections (xz slice through the center of the y axis) in the Chebyshev simulations at $t = 5$ days. Panel (a) shows the simulation with 64 vertical grid points while panel (b) shows the simulation with 128 vertical grid points for the case with $Ro = 0.05$. Velocity is normalized by 10^{-6}.

3.2.3 Energy Spectra

The horizontal kinetic energy spectra at the surface of the Chebyshev simulation for the cases with $Ro = 0.05$ are shown in figure 3.17 in panels (a) and (b). We see that there is somewhat less divergent energy present in the Cheb64 simulation compared to the Cheb128 simulation in the small-scales. This is to be expected due to the increased quantity of gravity waves seen in the plots of vertical velocity in figure 3.15. Furthermore, the slope of the Cheb64 run looks closer to a K^{-3} law while the Cheb128 simulation seems to be closer to a $K^{-5/3}$ law. Again, this may be a result of the increased resolution in the Cheb128 simulation. In panels (c) and (d) we show the energy spectra at $z/H \approx -0.1$ for the Cheb64 and Cheb128 cases with $Ro = 0.05$. The spectra look very similar to their corresponding Fourier simulation in figure 3.6. Between the Cheb64 and Cheb128 simulations we find a quite significant lack of divergent energy in the Cheb64 case at the smaller scales. This could be due to the relatively coarse resolution in the Cheb64 simulation that cannot resolve the smaller vertical length scales at this depth. Hence gravity waves propagating vertically are filtered out upon reaching the relatively coarse resolution in the interior. Similar to the Fourier simulation with $Ro = 0.05$ we find that divergent energy begins to dominate the rotational energy at the smallest resolved length scales.

Based on the Chebyshev simulations, we find that, while the Neumann vertical bound-

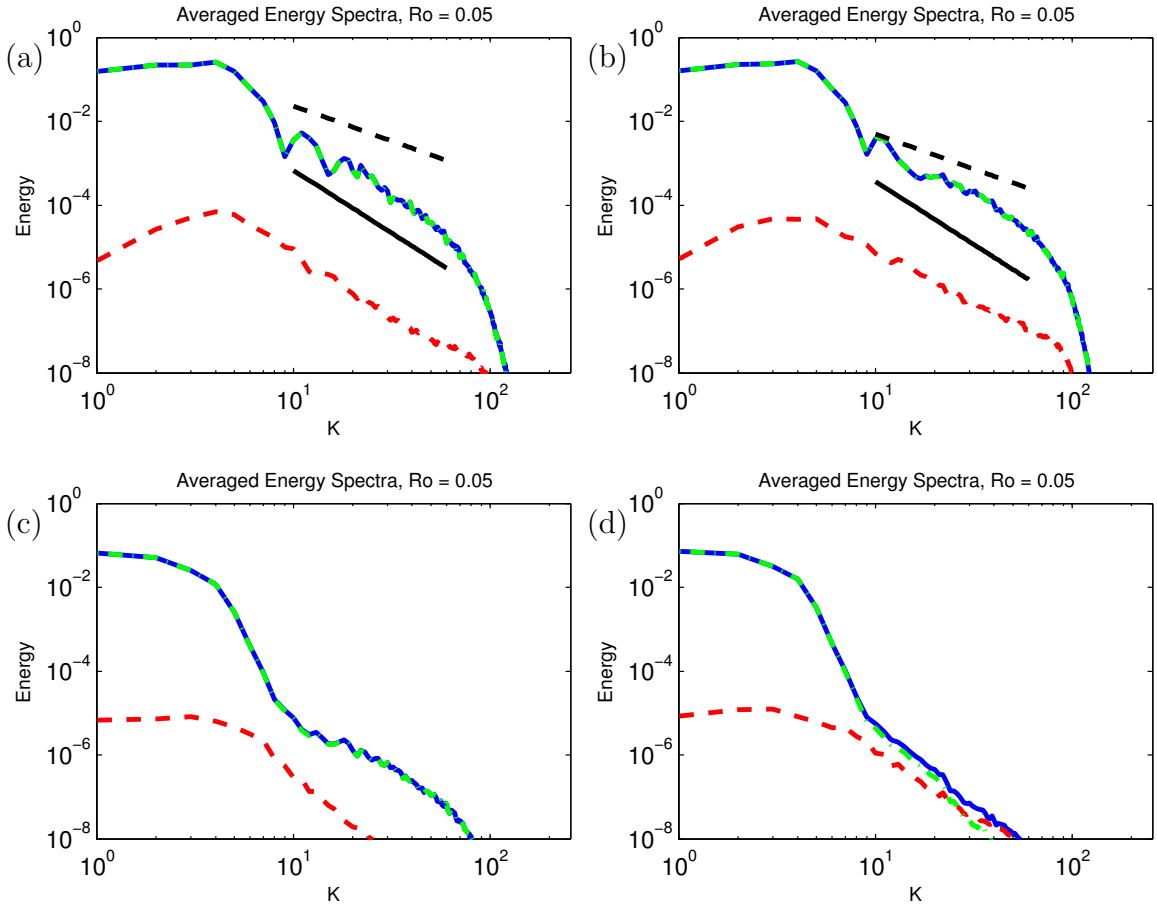

Figure 3.17: Energy spectra in the Chebyshev simulations. Panel (a) shows the spectra in the Cheb64 case with $Ro = 0.05$ and panel (b) shows the spectra in the Cheb128 case with $Ro = 0.05$. Panels (c) and (d) show the spectra at $z/H \approx -0.1$ in the Cheb64 and Cheb128 simulations, respectively.

ary condition in the Fourier simulations do generate QG PV, the discrepancy does not seem to affect the surface buoyancy evolution nor the generation of gravity waves. Indeed, we've seen that the Chebyshev simulations with the case $Ro = 0.05$ actually generate more gravity waves but qualitative features remain quite similar.

3.3 Non-Constant Buoyancy Frequency

In this section, we discuss some preliminary ideas regarding the case where the background stratification is non-linear, i.e. $N = N(z)$.

The advantage of having a constant buoyancy frequency, N, allowed one to find exact solutions for the streamfunction in equation (1.48). While there are $N(z)$ profiles which do allow for an exact solution, for example LaCasce 2006 [29] showed exact solutions can be found using an exponentially decaying $N(z)$ and Lindzen 1994 [34] showed that the profile,

$$N^2(z) = \frac{N_0^2}{1 - Dz}, \tag{3.6}$$

can also be solved analytically, in general, one must turn to solving the problem numerically.

As is often done for the ocean (e.g. [10], [24], [31]) we take the background stratification to have a pycnocline and define the buoyancy frequency to be

$$N^2(z) = N_0^2 + \alpha^2 \operatorname{sech}^2(\beta(z + p)), \tag{3.7}$$

where N_0^2 is the minimum buoyancy freqeuncy, α is a scaling parameter, β gives the width of the pycnocline, and p is the location of the pycnocline. As in the constant N case throughout the thesis, we set the interior QG PV to zero i.e. equation (1.48). To numerically solve (1.48), we use a centered second-order finite difference method and loop over all wavenumbers to find the solution in spectral space. We then use the inverse DFT to find the solution in physical space.

As discussed in section 1.1.3, one of the major assumptions in SQG is that $Bu \sim 1$. Since,

$$Bu = \left(\frac{N(z)H}{fL}\right)^2, \tag{3.8}$$

now depends on z, it can be difficult to ensure it is order 1 for all z in the domain. Therefore, one way to ensure that we choose a deep enough domain is to consider the minimum value $N(z)$ takes, i.e. $N_0 = 10^{-3}$ s^{-1}, and formulate the restriction in terms of that. We also fix $f = 10^{-4}$ s^{-1} and $L = 100$ km. To ensure $Bu \sim 1$, we take the depth of the domain to be 10 km.

In figure 3.18, we show a set of solutions to (1.48) using different parameter values of β and p down the middle of the horizontal domain. The initial surface buoyancy field remains the same as throughout the thesis: an elliptical vortex, described in detail during the beginning of chapter 3 (see equation (3.1)). Table 3.5 shows the full parameter values of

(3.7) used in solving (1.48). The first row of figure 3.18 shows a relatively thin pycnocline near the surface. As can be seen in the fourth column, the full buoyancy field has an area near the surface where the buoyancy decreases. This means that the initial setup is unstably stratified and thus we would find upwelling. This would detract from the pure SQG dynamics that we are trying to study. The second row has a wider pycnocline located near the surface. Here, the full buoyancy field is monotonically increasing as we move up from the bottom of the fluid and is an example of a suitable buoyancy profile for studying SQG. Finally, the third row has the same sized pycnocline as the first row, albeit deeper in the fluid. We can see that there is a slight decrease in buoyancy near the pycnocline. These solutions are meant to demonstrate the rich variety of initial setups that can be found using the buoyancy frequency profile, (3.7), in solving (1.48) for the steamfunction. It also demonstrates the difficulty that one can run into, in terms of choosing an initially stable buoyancy profile, when choosing parameter values in (3.7).

	N_0 [s^{-1}]	f [s^{-1}]	α [s^{-1}]	β [m^{-1}]	p [km]
First row	10^{-3}	10^{-4}	$33 \cdot 10^{-4}$	0.0025	1
Second row	10^{-3}	10^{-4}	$33 \cdot 10^{-4}$	0.00125	1
Third row	10^{-3}	10^{-4}	$33 \cdot 10^{-4}$	0.0025	3.5

Table 3.5: The full set of parameter values for the sample solutions to (1.48) shown in figure 3.18.

A first attempt at trying to understand how one can prescribe an initially stable buoyancy field is to consider scale analysis with $N = const.$ In particular, we know that if,

$$\frac{db}{dz} = N^2 + \frac{\partial b'}{\partial z} > 0, \tag{3.9}$$

then the fluid is initially stable. Since $N^2 >$ then an unstable buoyancy profile is possible if the vertical derivative of the buoyancy perturbations is negative (and at least the size of N^2 at that depth). The second term in (3.9) scales like,

$$\frac{db'}{dz} \sim \frac{fUL}{H^2}, \tag{3.10}$$

and therefore if one considers the ratio,

$$\frac{\frac{db'}{dz}}{N^2} \sim \frac{fUL}{H^2N^2} = \frac{U}{fL}\frac{f^2L^2}{N^2H^2} = \frac{Ro}{Bu}. \tag{3.11}$$

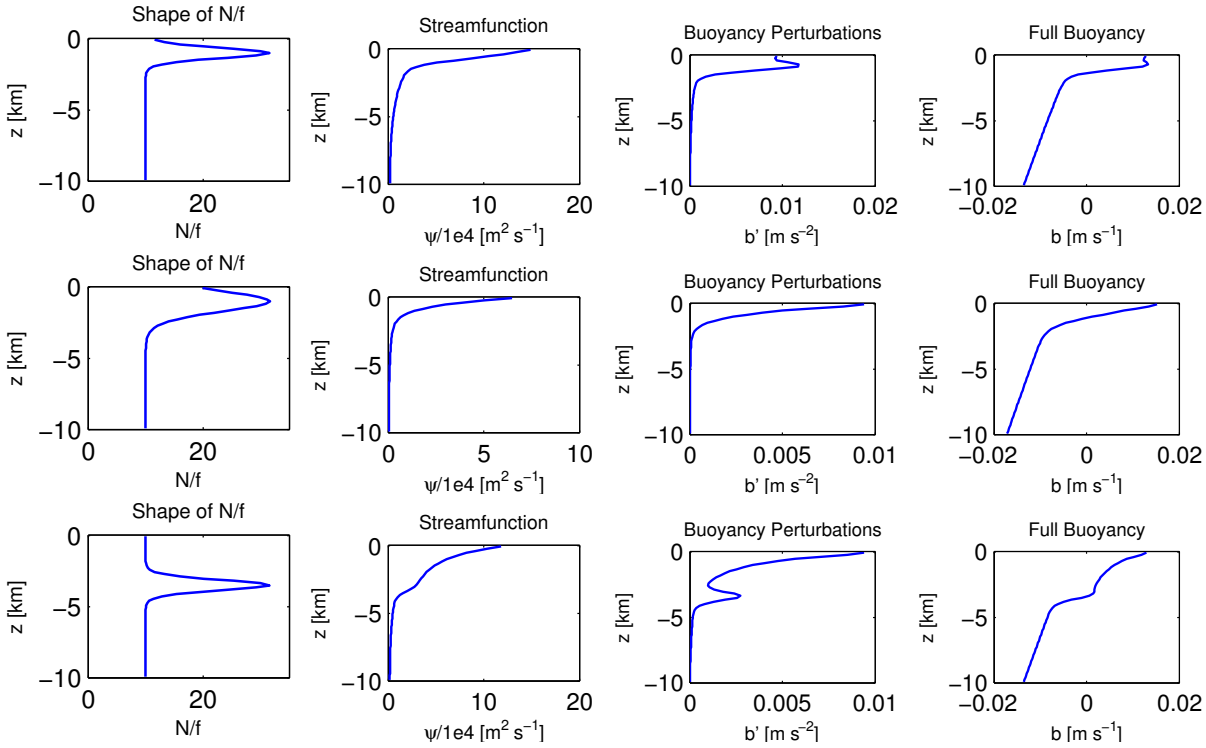

Figure 3.18: Solutions to (1.48) for buoyancy frequency defined in (3.7). Values of β and p are given in table 3.5. The first column is a plot of the ratio $N(z)/f$, second column shows the streamfunction solution, ψ, third column shows the buoyancy perturbation field, $b' = f\partial_z\psi$, and, finally, the fourth column shows the full buoyancy field $b = \bar{b}(z) + b'$.

Equation (3.11) suggests that if $Ro > Bu$, then the resulting initial buoyancy field may be unstable. Note that this is not a sufficient condition since we also require that $\partial_z b' < 0$.

The work on non-constant stratification is ongoing.

Chapter 4

Conclusions

This thesis investigated the range of validity of the SQG model in the context of a surface trapped elliptical vortex and how SQG breaks down at the small scales. While we only consider a single type of initial condition, we can hypothesize how the dynamics change as the Rossby number approaches unity.

For very small Rossby number, we find that the SQG model agrees quite well with the PE. This is most clearly seen in the evolution of the surface buoyancy field. However, as the Rossby number gets larger, dynamics begin to depart from the predictions of the SQG model. In particular, we find that the thin-filament instability, which is common in SQG, begins to stabilize. While the free-slip case with $Ro = 0.1$ used a stronger filter, the stabilization trend is clearly evident between the case with $Ro = 0.005$ to the case with $Ro = 0.05$. As well, the core of the vortex spreads out and becomes quite uniform as the Rossby number increases. The expanding of the vortex core also decreases the maximum magnitude of the surface buoyancy field.

While the prediction of the power law of the energy spectrum only really apply for a flow which is turbulent, we argue that there is still much to learn from discussing energy spectra of the surface trapped elliptical vortex. In particular, we have observed that the horizontal kinetic energy spectrum at the surface of the fluid in the elliptical vortex case changes as the Rossby number increases. The observed power law becomes steeper, indicating less energy in the small-scales which is reflected in the plots of the surface buoyancy, and more energy is transferred from the rotational modes to the divergent modes as the Rossby number increases. This increased divergent energy is seen through the emission of inertia-gravity waves from the vortex. While the case with $Ro = 0.005$ showed no clear evidence of gravity wave generation, it was found that the cases with $Ro = 0.05$ and $Ro = 0.1$ showed a large

amount of gravity wave generation. Suggested by Snyder et al. 2007 [40] this may be a result of using unbalanced initial conditions in a PE solver. We have also seen that in the case with $Ro = 0.05$, gravity waves seem to be generated very frequently, while the case with $Ro = 0.1$ suggests that gravity waves periodically generated. The difference in the vertical velocity fields between the two cases was an order of magnitude larger in the case with $Ro = 0.1$. The underlying reason for this is unclear but may have something to do with how large the local Rossby number becomes in the simulations.

We've also performed some resolution tests with a Chebyshev grid which only imposes no normal flow at the vertical boundaries. We find that, despite the spurious generation of QG PV near the surface, the Fourier solutions agree well with the Chebyshev simulations in terms of describing how the surface buoyancy field evolves. This is likely due to the fact that the vertical derivative of the buoyancy field is computed only during advection of vertical velocity which is quite small in magnitude. Comparing between 64 and 128 vertical grid points in the Chebyshev simulations we see quite large differences in vertical velocity field between the cases with $Ro = 0.05$. The dramatic increase in the quantity of gravity waves suggests that vertical resolution is extremely important. In fact, the vertical resolution in our simulations is often better than in other studies. For example, in Danioux et al. 2012 [10], vertical grid spacing ranges from 3 m near the sruface to 200 m at the bottom for a depth spanning about 4 km. In the Cheb64 and Cheb128 simulation for $Ro = 0.05$ whose depth spans 1 km, near the surface our resolution is 0.60 m and 0.15 m, respectively, to about 24 m and 12 m, respectively, in the interior. After re-scaling the depth in the simulation in Danioux et al. 2012 [10], their resolution is 0.75 m near the surface to 50 m near the bottom for a depth of 1 km.

Some preliminary ideas were also discussed for the scenario when $N \neq const.$ In particular, we've demonstrated that choosing appropriate parameter values to a setup that includes a pycnocline can be difficult to do since the initial buoyancy profile can be unstable. This initial instability of the buoyancy profile generates up-welling and detracts from a pure SQG study.

There are several directions in which one can pursue further research with the SQG model:

- Different initial conditions
- Non-constant buoyancy frequency
- Non-zero QG PV
- Varying Burger number or aspect ratio

First, perhaps the most obvious choice, one can change the initial conditions. In particular, our study focused on the elliptical vortex and, therefore, it is not immediately obvious whether the results can apply to other types of flows, for example, freely decaying turbulence. Second, as was briefly described in this thesis, one can study how dynamics change when we use a non-linear background stratification. The preliminary results discussed in this thesis would help in choosing parameter values that ensure a stable buoyancy field. This is a necessary step in order to study the SQG model since upwelling would detract from the dynamics in SQG. Using code written during this thesis one is able to generate the relevant initial conditions. In fact, some preliminary exploration of SQG with a pycnocline has already begun. Third, the SQG model assumes QG PV is zero everywhere. To improve our understanding of ocean dynamics one can incorporate QG PV into their setup (Tulloch and Smith 2009 [45] considered an SQG layer at the surface and bottom of the atmosphere and a barotropic and first baroclinic mode of QG PV) and simulate how the PE system evolves with this addition as the Rossby number changes. This would be a relatively simple problem to setup since the numerical solver QG3 can solve the SQG-QG system and setting up three-dimensional corresponding fields should be quite trivial. For SPINS, no changes to the underlying code would be required. However, we note that the use of the Chebyshev grid (which we feel gives a better description of SQG) would perhaps be unsuitable for an SQG+QG study. Since this setup would have vertically varying structures throughout the entire depth, the relatively coarse resolution in the interior of the Chebyshev grid could prove detrimental. Finally, we have only explored the SQG model in the context of varying Rossby number. However, as discussed in section 1.1.2, the SQG (and QG) model assumes that the Burger number is $O(1)$ and that the aspect ratio is very small. An exploration of varying Burger number or aspect ratio could similarly reveal novel dynamics not found in the SQG model.

References

[1] D.J. Acheson. *Elementary Fluid Dynamics*. Oxford Univeristy Press, 1990.

[2] G.K. Batchelor. *An Introduction to Fluid Dynamics*. Cambridge University Press, 1967.

[3] E. Bembenek, F.J. Poulin, and M.L. Waite. Realizing surface driven flows in the primitive equations. *Journal of Physical Oceanography*, 2014. Submitted.

[4] C.M. Bender and S.A. Orszag. *Advanced mathematical methods for scientists and engineers*. New York: McGraw-Hill, 1978.

[5] J.P. Boyd. *Chebyshev and Fourier Spectral Methods*. Courier Dover Publications, 2001.

[6] X. Capet, J.C. McWilliams, M.J. Molemaker, and A.F. Shchepetkin. Mesoscale to submesoscale transition in the california current system part iii: Energy balance and flux. *Journal of Physical Oceanography*, 38:2256–2269, 2008.

[7] X. Carton. Instability of surface quasigeostrophic vortices. *Journal of the Atmospheric Sciences*, 66:1051–1062, 2009.

[8] J.G. Charney. On the scale of atmospheric motion. *Geofys, Publikasjoner*, 17(2):1–17, 1948.

[9] J.G. Charney. Geostrophic turbulence. *J. Atmos. Sci.*, 28:1085–1095, 1971.

[10] E. Danioux, J. Vanneste, P. Klein, , and H. Sasaki. Spontaneous inertia-gravity-wave generation by surface-intensified turbulence. *J. Fluid Mech.*, 699:153–173, 2012.

[11] P.A. Davidson. *Turbulence*. Oxford Univeristy Press, 2004.

[12] D.G. Dritschel. An exact steadily rotating surface quasi-geostrophic elliptical vortex. *Geophysical and Astrophyiscal Fluid Dynamics*, 105(4-5):368–376, 2011.

[13] D.R. Durran. *Numerical Methods for Wave Equations in Geophysical Fluid Dynamics*. Springer, 1999.

[14] M. Frigo and S.G. Johnson. The design and implementation of FFTW3. *Proc. IEEE*, 93(2):216–231, 2005.

[15] T. Frisius. The development of a cyclone-anticyclone asymmetry within a growing baroclinic wave. *Journal of the Atmospheric Sciences*, 60, 2003.

[16] A.E. Gill. *Atmosphere-Ocean Dynamics*. Academic Press, 1982.

[17] G.J. Hakim, C. Snyder, and D.J. Muraki. A new surface model for cyclone-anticyclone asymmetry. *J. Atmos. Sci.*, 59(16), 2002.

[18] B.J. Harvey and M.H.P. Ambaum. Instability of surface-temperature filaments in strain and shear. *Quarterly Journal of the Royal Meteorological Society*, 136:1506–1513, 2010.

[19] I.M. Held, R.T. Pierrehumber, Garner S.T., and K.L. Swanson. Surface quasi-geostrophic dynamics. *J. Fluid Mech.*, 282:1–20, 1995.

[20] B.J. Hoskins, I. Draghici, and H.C. Davies. A new look at the omega-equation. *Quarterly Journal of the Royal Meteorological Society*, 104:31–38, 1978.

[21] M.Y. Hussaini, D.A. Kopriva, and A.T. Patera. Spectral collocation methods. *Applied Numerical Mathematics*, 5:177–208, 1989.

[22] J. Isern-Fontanet, G. Lapeyre, P. Klein, B. Chapron, and M. Hecht. Three-dimensional reconstruction of oceanic mesoscale currents from surface information. *Journal of Geophysical Research: Oceans*, 113:153–169, 2008.

[23] M. Juckes. Quasigeostrophic dynamics of the tropopause. *Journal of the Atmospheric Sciences*, 51(19):2756–2768, 1994.

[24] P. Klein, B.L. Hua, G. Lapeyre, X. Capet, S. Le Gentil, and H. Sasaki. Upper ocean turbulence from high-resolution 3d simulations. *Journal of Physical Oceanography*, 38:1748–1763, 2008.

[25] P. Klein, J. Isern-Fontanet, G. Lapeyre, G. Roullet, E. Danioux, B. Chapron, S. Le Gentil, and H. Sasaki. Diagnosis of vertical velocities in the upper ocean from high resolution sea surface height. *Geophysical Research Letters*, 36, 2009.

[26] A.N. Kolmogorov. The local structure of turbulence in incompressible viscous fluid for very large reynolds numbers. *Proceedings: Mathematical and Physical Sciences*, 434(1890), 1941.

[27] P.K. Kundu and I.M. Cohen. *Fluid Mechanics*. Academic Press, 2010.

[28] J.H. LaCasce. Surface quasigeostrophic solutions and baroclinic modes with exponential stratification. *Journal of Physical Oceanography*, 42:569–580, 2012.

[29] J.H. LaCasce and A. Mahadevan. Estimating subsurface horizontal and vertical velocities from sea-surface temperature. *Journal of Marine Research*, 64:695–721, 2006.

[30] G. Lapeyre. What vertical mode does the altimeter reflect? on the decomposition in baroclinic modes and on a surface-trapped mode. *Journal of Physical Oceanography*, 39:2857–2874, 2009.

[31] G. Lapeyre and P. Klein. Dynamics of the upper oceanic layers in terms of surface quasigeostrophy theory. *Journal of Physical Oceanography*, 36:165–176, 2006.

[32] P.Y. Le Traon, P. Klein, B.L. Hua, and G. Dibarboure. Do altimeter wavenumber spectra agree with the interior or surface quasigeostrophic theory? *Journal of Physical Oceanography*, 38:1137–1142, 2008.

[33] M. Lesieur. *Turbulence in Fluids*. Springer, 2008.

[34] R.S. Lindzen. The eady problem for a basic state with zero pv gradient but $\beta \neq 0$. *J. Atmos. Sci.*, 51:3221–3226, 1994.

[35] M.J. Molemaker, J.C. McWilliams, and X. Capet. Balanced and unbalanced routes to dissipation in an equilibrated eady flow. *J. Fluid Mech.*, 654:35–63, 2010.

[36] G.D. Nastrom and K.S. Gage. A climatology of atmospheric wavenumber spectra of wind and temperature observed by commercial aircraft. *Journal of the Atmospheric Sciences*, 42(9):950–960, 1985.

[37] R.T. Pierrehumbert, I.M. Held, and K.L. Swanson. Spectra of local and nonlocal two-dimensional turbulence. *Chaos, Solitons and Fractals*, 4(6):1111–1116, 1994.

[38] C.B. Rocha, A. Tandon, I.C.A da Silveira, and J.A.M. Lima. Traditional quasi-geostrophic modes and surface quasi-geostrophic solutions in the southwestern atlantics. *Journal of Geophysical Research: Oceans*, 118:2734–2745, 2013.

[39] R. Rotunno, D.J. Muraki, and C. Snyder. Unstable baroclinic waves beyond quasi-geostrophic theory. *J. Atmos. Sci.*, 57, 2000.

[40] C. Snyder, D.J. Muraki, R. Plougonven, and F. Zhang. Inertia-gravity waves generated within a dipole vortex. *J. Atmos. Sci.*, 64, 2007.

[41] C.J. Subich, K.G. Lamb, and M. Stastna. Simulation of the navier-stokes equations in three dimensions with a spectral collocation method. *Int. J. Numer. Meth. Fluids*, 73:103–129, 2013.

[42] L.N. Trefethen. *Spectral Methods in MATLAB*. SIAM, Philadelphia, 2000.

[43] R. Tulloch and K.S. Smith. A new theory for the atmospheric energy spectrum: Depth-limited temperature anomalies at the tropopause. *PNAS*, 103(40):14690–14694, 2006.

[44] R. Tulloch and K.S. Smith. A note on the numerical representation of surface dynamics in quasigeostrophic turbulence: Application to the nonlinear eady model. *Journal of the Atmospheric Sciences*, 66:1063–1068, 2009.

[45] R. Tulloch and K.S. Smith. Quasigeostrophic turbulence with explicit surface dynamics: Application to the atmospheric energy spectrum. *Journal of the Atmospheric Sciences*, 66:450–467, 2009.

[46] G.K. Vallis. *Atmospheric and Oceanic Fluid Dynamics: Fundamentals and Large-Scale Circulation*. Cambridge University Press, 2006.

[47] A. Venaille, G.K. Vallis, and K.S. Smith. Baroclinic turbulence in the ocean: Analysis with primitive equation and quasigeostrophic simulations. *Journal of Physical Oceanography*, 41:1605–1623, 2011.

[48] M.L. Waite. Course notes for AM900: Instability and turbulence.

[49] M.L. Waite and P. Bartello. The transition from geostrophic to stratified turbulence. *J. Fluid Mech.*, 568:89–108, 2006.

[50] J.S. Whitaker. A comparision of primitive and balance equation simulations of baroclinic waves. *J. Atmos. Sci.*, 50(11), 1993.